

https://dspace.org/

The physical and numerical modelling of fracture growth in underground excavations.

Tomlin, Wayne

1998
https://hdl.handle.net/10539/27351

Downloaded from a DSpace repository. https://dspace.org/

The Physical and Numerical Modelling of Fracture Growth in Underground Excavations

Wayne Tomlin

A dissertation Submitted to the Faculty of Engineering, University of the Witwatersrand, Johannesburg for the degree of Master of Science.

Johannesburg 1998.

Declaration

I declare that this is my own, unaided work. It is being submitted for the Degree of Master of Science in Engineering in the University of the Witwatersrand, Johannesburg. It has not been submitted for any degree or examination in any other university.

Signed this 21st day of April 1998

Wayne Tomlin

Abstract

In the field of numerical modelling in rock mechanics, one of the main hindrances is the limited knowledge of the mechanisms of fracturing and failure in brittle rock. A way to increase this knowledge of rock behaviour is by carrying out laboratory experiments under controlled conditions.

The Displacement Discontinuity Method, capable of fracture growth simulation (DIGS), has been used to model fracturing of deep level underground excavations. In addition to an ordinary underground mining simulation, certain geological structures have been simulated and there influence on fracturing. The main objective of this dissertation is to verify and calibrate DIGS by comparing results of physical experiments and numerical simulations.

Comparing the results of the laboratory experiments and the numerical simulations of these simulations, it has been possible to define the basic failure mechanisms around a deep level stope, and the influence of certain geological structures. The samples used to do the simulations were machined out of Quartzite, Black Reef Quartzite and Norite. The tests were carried out in a biaxial cell, which was built especially for these tests.

When mining in a solid block with no geological structures present, the effect of stope closure caused very different fracture formations when compared with the no stope closure case. When closure of the stope occurred, the fractures formed ahead of the face

and shear fractures were formed. When closure of the stope did not take place, the fractures formed behind the face and the nature of the fractures were mainly tensile. DIGS correctly simulated the same fracture pattern as was found in the physical experiments.

When simulating the effect of a discontinuity was carried out, fracturing tended to extend into the discontinuity, but not through the discontinuity. Evidence of activation of the discontinuity was found. Simulating the effect of parting planes on fracture formation led to the initiation of tensile fractures ahead of the face at the parting planes interface. These results were obtained in both physical and numerical simulations.

The comparison between the physical experiments and the numerical simulations has shown favourable results indicating that DIGS can correctly simulate fracture initiation, fracture growth, stress conditions and stress redistribution.

Contents	Page
Declaration	ii
Abstract	iii
Contents	v
List of figures	viii
List of tables	xi
1. Introduction	1
2. Literature Survey	4
2.1 Fracturing around deep level stope	4
2.2 General Characteristics	13
2.3 Physical Modeling	16
2.4 Numerical Modeling	23
3. Failure in Brittle Rock	32
4. Experimental Setup	41
4.1 Biaxial Load Cell	41
4.2 Specimens	43
4.3 Data Acquisition	43
4.4 Testing Procedure	45
5. Analysis of fracture formation during elastic closure	47
5.1.1 Stress strain data for the case of no closure	54
6. Fracture formation when mining in a solid block	55
6.1 Displacement versus Load	60
6.1.2 Stress vs strain	61

6.2 Orientation of fractures 64

6.3 Results from DIGS tesselation 65

6.3.1 Poission's Ratio 65

6.3.2 Young's Modulus 66

6.3.3 Mobilised Cohesion 69

6.3.4 Unmobilised cohesion 69

6.3.5 Conclusions about DIGS tesselation 72

7. Effect of a discontinuity on the final fracture formation 73

7.1 Physical Models 73

7.2 Numerical Simulations 76

7.3 Comparison of Physical and Numerical Models 79

7.4. Comparing step by step outputs of Physical and numerical models 80

7.5 Simulated orientation of stresses 86

8. Influence of Parting Planes on fracture formation around a deep level stope 88

8.1 Physical Model 88

8.1.1 Acoustic emission 88

8.2 Numerical Simulations 90

8.3 Comparison of physical and numerical models 93

8.4 Observation of principle stress direction 96

8.5 Fracture initiation 97

9. Conclusion and Recommendations 99

10. References 103

11. Appendix A 105

List of Figures **Page**

Figure 2.1.1 Diagram of the fracture zone around a stope face showing type 1, 2 and 3 fractures. 5

Figure 2.1.2. A schematic of fracture distribution around a stope face. 9

Figure 2.3.1. Fracture patterns around rectangular slits in quartzite, arrows parallel to bedding planes. 18

Figure 2.3.2. Fracture patterns around rectangular slits in Sandstone 20

Figure 2.3.3. Schematic representation of the fracture pattern observed from the vertical sections taken from laboratory pillar-stope test specimens under biaxial loading conditions. 21

Figure 2.3.4. Schematic representation of the fracture pattern around a stope. 22

Figure 2.4.1. Numerical simulations of a deep underground stope 24

Figure 2.4.2. Simulating fracture growth using tensile fracture growth rule. 25

Figure 2.4.3. Simulating fractutre growth using the shear growth Rule. 26

Figure 2.4.4. Fracture pattern after 14 mining steps of 1m in a uniform rockmass. 28

Figure 2.4.5. The effect of parting planes on the fracture pattern around a stope with high friction angles. 29

Figure 2.4.6. The effect of parting planes on the fracture pattern around a stope with low friction angles. 29

Figure 2.4.7. Fracture initiation in a stope with a set of steeply dipping joints in the hangingwall. 30

Figure 3.1. Mohr-Coulomb envelope 32

Figure 3.2. Local coordinate system used to evaluate critical field values to determine fracture propagation directions. 34

Figure 4.1. A schematic of the biaxial cell used for the physical Experiments. 42
Figure 4.2. A typical test specimen geometry. 44

Figure 5.1. Graph showing closure profiles for stoping widths of 0.2mm, 0.5mm, and 2mm. 48

Figure 5.2. The fracture patterns observed from testing and modeling. 53

Figure5.1.1 Stress strain data for the case for no closure 54

Figure 6.1. Fracture patterns obtained from DIGS for the "solid block" case. 58

Figure 6.2. Comparison of the "solid block" experiments at the Seventh mining step. 59

Figure 6.1.1.1 Displacement versus load curve. 60

Figure 6.1.2.1. Stress versus strain curve 61

Figure 6.2.1. DIGS output showing principle stress directions. 64

Figure 6.3.1.1. DIGS output from DIGS tesselation showing the effects of varying the Poisson's ratio. 67

Figure 6.3.2.1 DIGS output from DIGS tesselation showing the effects of varying the Young's Modulus. 68

Figure 6.3.3.1. DIGS output from DIGS tesselation showing the effects of varying the Mobilised cohesion. 70

Figure 6.3.4.1. DIGS output from DIGS tesselation showing the effects of varying the Unmobilised cohesion. 71

Figure 7.1.1. A schematic of fracture patterns observed in physical models. 75

Figure 7.2.1. Fracture patterns predicted in numerical simulations. 78

Figure 7.3.1. Step-by-step comparison of the physical experiments Versus numerical simulations. 85

Figure 7.4.1. Output from DIGS simulating the stress directions with an existing discontinuity. 87

Figure 8.1.1. Schematic of fracture patterns observed in physical models using black reef quartzite. 89

Figure 8.1.1.1. Locations of accoustic emissions determined in

physical models using black reef quartzite. 91

Figure 8.3.1. Fracture patterns predicted in numerical simulations of black reef quartzite. 92

Figure 8.4.1. DIGS output of principle stress directions with an existing parting plane. 96

Figure 8.5.1. Stress versus strain data for the parting plane sample 98

List of Tables **Page**

4.1 Material properties of the rock types used for the experiments 43

5.1 Summary of the types of tests conducted 47

I Introduction

Simulating fracture zones induced by tabular excavations in deep level mines would have major benefits for the mining industry. Once this is achieved, fracture patterns can be generated numerically, and used to infer the state of stress in the stope fracture zone. The in turn would lead to improved methods of modelling and designing the interaction between support units and the fracture zone and the ability to evaluate rock engineering strategies such as caving and stope face pre-blasting. However, one of the major impediments in the field of numerical modelling in rock mechanics is the limited knowledge of the mechanisms of fracture and failure of brittle rock. Improving the understanding of rock behaviour and developing better numerical models are an interactive process and the two need to be continually checked and validated against each other. Physical information obtained in situ is preferred, but in many, this is difficult because of the difficulties involved in describing the rock mass structure and determining forces in situ. However, understanding the nature of the fracture zone has not been entirely unsuccessful and a conceptual understanding has been built up over the years. This has been compiled from the mapping of fractures exposed on the hangingwalls of the stopes and on the sidewalls of gullies and tunnels advanced ahead of the mining face along with from observation of fractures intersecting boreholes drilled from tunnels below stopes at different angles into the stope face.

Testing models under controlled conditions in the laboratory is probably a better option for initial calibration and validation of numerical models and constitutive laws as well as studying the process of fracture initiation and growth.

The second chapter of this dissertation includes a literature survey. This includes an understanding of the fracture zone in a deep level underground stope and how the fractures form and the mechanisms of fracture formation. The published finding of many authors have been used to describe the fracture formation process. The literature survey also includes work done previously on physical testing in the laboratories of similar works done on a similar topic. A brief discussion of the outputs from the various authors and the conclusions which could be useful in explaining certain factors. Finally the literature survey looks at previous work done on the numerical simulation of similar geometry's and their results.

Chapter three describes the mechanism causing fracturing in brittle rock. The numerical model uses these mechanisms with some modifications. The modifications are described in chapter three. Also, a decision had to be made as to which numerical model was going to be used for the numerical simulations. Chapter three looks at the different options, briefly describing each numerical model and finally it describes why DIGS was chosen as the model to be used.

Chapter four deals with the experimental setup and the development of certain equipment. Chapter four includes the dimensions and the machining of the samples as well as describing the method used in carrying out the physical test.

Chapter five, six, seven and eight deals with the results of each individual set of tests which were carried out. Chapter five deals with the effect of closure on the final fracture pattern, chapter six the fracture pattern obtained from mining in a solid block, chapter seven deals with the influence that a discontinuity had on the final

fracture pattern and finally chapter eight, which deals with the influence that parting planes had on the final fracture pattern. Each of these chapters include a comparison between the fracture patterns of the physical experiments the results from previous authors. Chapter nine has conclusions and recommendations.

II Literature Survey

The majority of this dissertation deals with the fracture zone around a deep level stope. It is therefore necessary to review the current beliefs of the fracture zone. This literature survey looks at a number of theories which have been published.

2.1 Fracturing around a deep level stope face

According to Joughin and Jager (1984) fractures around a stope are classified into categories according to their inclination, the presence or absence of movement across the fractures and on the secondary structures associated with the fractures.
Joughin and Jager proposed that there were three types of fractures and that these fractures strike substantially parallel with the stope face.

Type 1 Fractures

According to Joughin and Jager (1984), the most common fracture are the type 1 fractures, labeled 1 in figure 2.1.1.. These fractures are planar, steeply inclined, and have no displacement in the plane of the fracture when they are first formed. However, the inclination of these fractures vary. The inclination varies according to the amount of energy being released in the stope or the span of the stope. When large spans occur these type one fractures are steeply inclined. Joughin and Jager (1984) found the inclination of these angles to be between 80 and 100 degrees to the horizontal. For the case of shorter spans, the fractures in the immediate hanging and footwall were found to be if a shallower angle, compared to the angle of the wider

span, and were in the direction of face advance. Joughin and Jager (1984) found that the rate at which stress was being released in the stope affected the distance the fractures were being formed ahead of the stope face. They found that these fractures were being formed several meters ahead of the stope face and in zones, each zone consisting of 5 to 20 fractures and separated from its neighboring zone by a width of intact rock. In later stages of the development of the fracture zone, as the face approaches close to the fractures formed previously, more fracturing occurs to form parallel sided slabs and small angled wedges of rock.

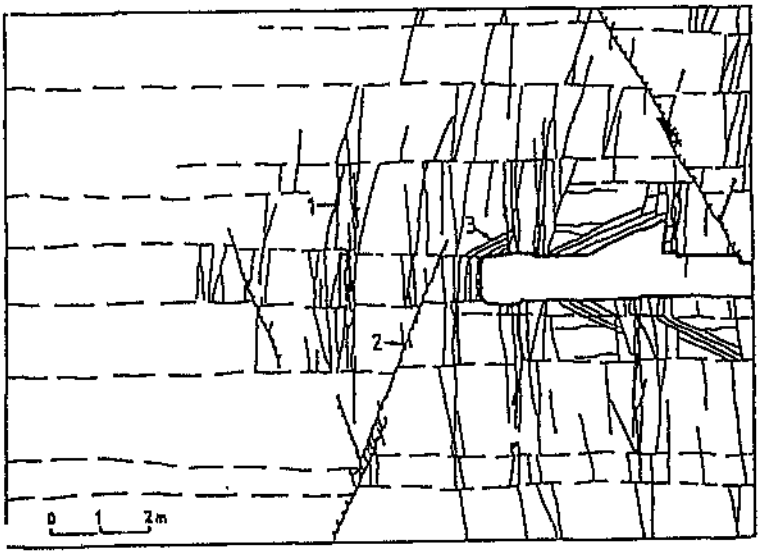


Figure 2.1.1. Diagram of fracture zone around a stope face showing type 1, 2 and type 3 fractures.

Their findings showed that closure of the stope, although not total closure, caused movements between the slabs and the horizontal movement of rock towards the stope. This movement caused communition along the fracture surfaces and secondary small cross fractures from type 1 fractures which left the rock in a cataclastic condition. At their time of formation, these type 1 fractures were almost always found to be in the direction of the major principle stress. Literature has shown if the fractures are tensile fractures. Joughin and Jager (1984) [illegible] virgin stress measurements directly ahead of a stope because of the [illegible] with the borehole discing of the core.

Type 1 fractures are tensile fracture and occur in all stopes where the stresses are stresses are high enough to cause fracturing . The amount of these fractures which occur increases as the rate at which energy in the stope is released increases. Type 1 fractures seldom grow through a parting plane, but have been known to do so.

Type 2 fractures

These fractures were found by Joughin and Jager (1984), to be far less common than type 1 fractures and are inclined at angles of 60 to 75 degrees to the horizontal. These fractures are labeled 2 in Figure 2.1.1. They have a component of displacement up to 150 mm in the plane of the fracture and can be quite complex. In their simplest, they are a few millimeters. The fracture zone is filled with highly comminuted material indicating the presence of a shearing action. This zone is several centimeters in width. The larger fractures have been traced for 30 meters along strike, and several

meters out of the plane of the reef. These shear fractures are formed when the minimum principal stress at failure is much higher than when fractures resembling extension or type 1 fractures are formed. This would imply that type 2 fractures are formed underground and in circumstances where the confining stress are high. Type 2 fractures are formed without noticeable seismic activity.

Type 3 Fractures

Type 3 fractures are inclined between 20 and 40 degrees to the horizontal towards the direction in which the face is advancing. This is shown as number 3 in Figure 2.1.1. they are clean planar fractures which display no evidence of shear displacement are confined to the first few strata above and below the stope, and seldom have strike lengths greater than 5 mm. These flat extension fractures form close t the stone face within rock. They develop in previously intact zones separating the fracture zones which formed several meters ahead of the face. Therefore, type 3 fracture second generation of fractures superimposed on the more regional fracture pattern. They occur in response to the very localised stress changes at the outer surface in fractured rock from the fracture zone towards the mind out area.

Another theory about the classification of fractures around a stope was published by Brummer and Rorke (1984). They believe that by mapping the mining-induced fractures a better understanding of the failure and deformation mechanisms producing these fractures could be obtained. In this theory, the fracture zone is categorized in two zones.

To obtain a better understanding of the fracturing around a deep level stope, and obtain ideas about the mechanisms of failure, it is important that this theory be closely studied. A graphic representation of this theory can be seen in Figure 2.1 2.

Zone 1

This zone is the zone furthest away from the stope face. The boundary between the fractured rock and the intct rock forms zone 1. This zone is subjected to the highest stresses and is the position at which the fracturing of rock first occurs. According to Brummer and Rorke (1984) who have carried out a number of laboratory experiments, the sequence of fracture formation of microscopic tensile 'splits', originating within individual grains in the matrix, joining of these microfractures into a narrow steeply inclined plane, and subsequent shear displacement along the overall inclined plane.

Due to the concentration of these microfractures in a narrow plane of weakness, these shear planes separate the rock into distinct blocks of relatively intact rock and Parallel to the overall longwall direction and result in an initial dilation of the rock towards the stope.

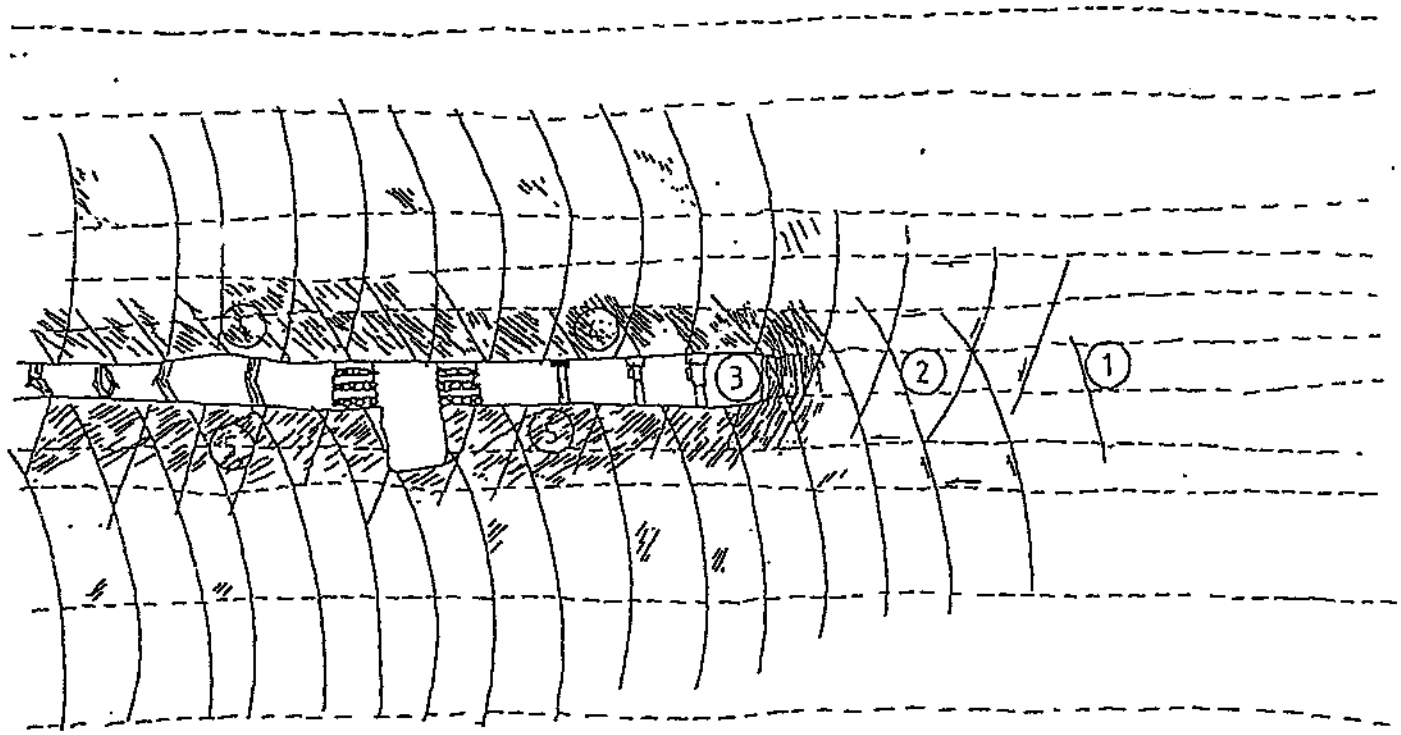


Figure 2.1.2 A Schematic of Fracture Distribution around a Stope Face (Brummer & Rourke, 1984)

Zone 2

This zone is described as the zone which is subjected to moderate vertical stress. The rock in this zone is described as being in a state of failure. Rock in this zone has negligible amount of cohesion along any fracture. The type of fracturing in zone two is made up of two different mechanisms. Firstly, on the microscopic scale, movements caused by the shear planes described in zone 1 causes the rock to break into wedge shaped interlocking pieces. Secondly, on the interblock scale, local high stresses at asperities and other points of contact cause individual blocks to split in the direction of the maximum principle stress. These fractures are therefore extension fractures with little relative displacement. These fractures can be compared to the type 1 fractures as described by Joughin and Jager (1984). Brummer and Rorke (1984) had similar findings to Joughin and Jager (1984) with regards the movement of the rock mass in the solid unmined area towards the mined out area along the parting planes. This would suggest that there is very little friction on the parting planes, and that mobilisation of these planes is easy. This is important later in this dissertation when numerical simulations are carried out on samples which contain parting planes. The figures used to describe the parting planes' characteristics should be similar to what is described above.

Zone 3

In this zone, local longitudinal splitting of the rock occurs in the direction of the maximum principle stress. These fractures are extension fractures. This zone is ot the immediate stope face which is often the site of slabbing. This slabbing takes place because of these longitudinal fractures.

Zone 4

Zone 4 begins at the hangingwall surface of the stope and the first active parting place above the stope. It consists of fractured layers of rock. Brummer and Rorke (1984) point out that the stresses in this zone depend on the support techniques and the lo9cal excavation geometry. The reason for this being that the vertical stresses in this zone are very low, however, the horizontal stresses can be very high.

Zone 5

Zone 5 is described as being the same as zone 4, except that it is from the footwall boundary down to the first acti[illegible]ting plane.
Brummer and Rorke (1984) and Joughin and Jager (1984) had similar findings with regards the shallow dipping fractures near to the face in both the hangingwall and footwall. These fractures are formed due to the high horizontal stresses build up around the stope. These stresses are caused by the rock ahead of the stope face wanting to move into the mind out area. A way of reducing the horizontal stresses

would be to carry out some excavations in the hangingwall or in the footwall as these excavations serve to relax the horizontal stresses in the strata.

Brummer and Rorke (1984) observed that the shear fractures in zone 1 can be separated into two families. The shear fractures in the hangingwall dip towards the mined-out area while the fractures in the footwall dip away from the mined-out area. This can be explained by these two families being superimposed on one another near the plane of the reef to form conjugate pairs. Conjugate pairs are usual for material failing in shear.

Experiments carried out by Legge (1986) on the fracturing ahead of the stope face also agrees with the findings of Brummer and Rorke (1984). Legge (1986) found that the rock was fracturing in shear several meters ahead of the face. This is due to the highly confined environment that the fractures are being formed in. Secondly, Legge (1986) found the formation of highly dilatant secondly fracture close to the face. The change from shear fractures a few meters ahead of the stope to extension fractures close to the face is mainly because of the change in the confining stresses. With high confining stresses a few meters from the stope face as opposed to the highly reduced confining stresses close to the face. This area of fracturing is described by Brummer and Rorke (1984) as zone 3 (figure 2.1.2). Legge's (1986) findings are the same with the occurrence if vertically orientated fracturing which dip towards the stope in the hangingwall and footwall, The fractures were found to follow the direction of the maximum principle stress. The fractures in this region resulted in narrow parallel sided slabs of rock. All of these findings are consistent to those of Brummer and Rorke (1984).

2.2 General characteristics of the fracture zone

Once all the factors influencing the formation of the fracture zone have been taken into account, the fracture zone around a stope face shows a systematic pattern of behaviour.

For the purpose of this dissertation, it is necessary to understand the main features of the fracture zone surrounding a stope face in a deep level mine. Features which are briefly discussed are the development of the fracture zone, dimensions of the fracture zone, arrangement of fractures in the fracture zone, displacement if fractured rock within the fracture zone and the influence of Geological structures on the fracture zone.

2.2.1 Development of the fractured zone

Most of the fractures develop in direct response to the mining of the stope face. Therefore it follows that as the stope advances, so the fracture zone advances, ahead of the face. The formation of this fracture zone is stable without the release of much seismic energy.

2.2.2 Dimensions of the fracture zone

The distance ahead of the stope that is fractured is very dependent on the amount of stress which is released within the stope. This distance may however be affected to a lesser extent by the rock type. Fracture may extend between 1 and seven meters into the face, depending on the amount of stress which is being released in the stope. For

relatively small amount of stress being released, the fractures will only be formed a short distance ahead of the face, while for large amounts of stress being released, this distance will increase.

A full understanding of distance to which fracturing occurs above and below the stope has not yet been established. However, it is thought that this distance of fracturing is also linked to the amount of energy being released within the stope.
The intensity of fracturing around a stope decreases as the distance from the stope increases.

2.2.3 Arrangement of fractures in the fracture zone

Most of the fractures around the stope are parallel to the stope face. Where there are changes in the direction of the face, for example a corner abutment, the fracture will follow the face around the corner. However, at the apex of the corner, the fractures will follow a curved path around the corner. This would suggest the direction of the maximum principal stresses. This changing in the direction of the fractures will only occur for major changes in the direction of the face and not for small irregularities in the face. For regular deviations in the shape of the face for example in a step-like pattern between successive panels on a longwall, long pronounced extension fractures will follow the overall shape of the face. The extension fractures ahead of the face, cluster in bands which are separated from each other by relatively unfractured rock. The spacing between these bands of clustered fractures is affected by factors such as stope height and the type of roof support used.

2.2.4 Displacement of fractured rock within the fracture zone

In the vertical direction, there is considerable motion along the shear fractures. This would be expected as shear fractures form as a result of a shearing motion and displacement is often a result. Much movement takes place in the horizontal direction as well. The fractured rock from the solid area moves towards the mined out area. This displacement of rock starts occurring slightly ahead of the fracture zone. This is where the rock is approaching the state of failure. When the rock does fail, dilation occurs due to the formation of fractures. Nearer the face, the already formed fractures now dilate even more resulting in the horizontal displacement in the fracture zone. The rock in between two dilating regions undergo little fracturing and merely move towards the mined out area.

Horizontal motion towards the mined out area also takes place through the rotation of slabs of rock which are created by the extension fractures in the immediate hangingwall and footwall. This motion becomes evident if gullies are cut parallel to the face in the hangingwall or footwall. This motion could also have an effect on the development of fractures in the fracture zone as it would cause a change in the confining forces on the rock undergoing failure.

2.2.5 Influence of Geological structures on the fracture zone

Dykes, faults and joints have a large effect on the development of the fracture zone. The orientation of these fractures with respect to the stope face is important as they affect the stress characteristics and therefore the fracture zone surrounding the tope

face. Their effects are least when they are at right angles to the face and greatest when parallel to it. Where there is closely spaced, parallel, open jointing there is little or no mining-induced fracturing.

The density of fracturing on one side of a fault is sometimes different to the density of fracturing on the other side. This could be explained by the possible abnormal tectonic stresses in the vicinity of the fault or discontinuity. Another explanation could be the altering of the induced stress due to the orientation of the fault relative to the direction of the face. These alterations in the induced stresses and therefore the natural stable formation of the fracture zone could be significant in causing unstable failure because they allow the build up of abnormally high stresses.

2.3 Physical Modeling

This dissertation deals with the physical modelling of underground excavations. It is necessary therefore to look at previous work done in this area. N.C. Gay (1972) carried out some experiments in the laboratory on fracture growth with rectangular openings. There are to distinct differences in Gay (1972) tests as opposed to the tests done in this dissertation. The samples of Gay (1972) samples were of cylindrical shape and the stress conditions were hydrostatic, while for the tests in this dissertation, the samples are of cubic shape, and the stress conditions are triaxial. The experiments carried out by Gay (1972) experiments consisted of two series of five tests. The first test in the first series being subjected to the lowest pressure. The second test were subjected to the same pressure as the first test, but for a much longer time interval. This would illustrate the effect of the time dependence nature of the formation of the fracture zone. The third test was subjected to double the pressure of

the first and second tests, and was also held at the pressure for some time. The fourth test was subjected to high pressure conditions and the final test was subjected to extreme pressure conditions with an increased axial ratio. The results of these tests are now briefly discussed. Figure 2.3.1. shows the results of the tests carried out. Figure 2.3.1. (a), (b), (c), and (d) being tests 1, 2, 3, and 5 respectively. In test 1, the corners were still clearly defined, expect for one fracture which went from one of the corners of the excavation, parallel to the bedding plane. This sample failed along this fracture. Very little cracking occurred. In the second test carried out by Gay (1972), the corners of the excavation were rounded off, a zone of spalling formed and fracturing extended into the sample for a distance of between one and two millimeters. Bedding planes were enhanced, and fractures parallel to the bedding planes were constant. The shear zone in the spalled zones, tended to run parallel to the bedding planes. In these shear zones, fracturing cut through individual grains both in the harder minerals of quartz and pyrite and in the weaker minerals of chlorite and sericite. In the third test, an increase in the intensity of cracking in the spalled zone occurred. Fracturing ahead of the excavation extended for more than two millimeters. Bedding planes were again enhanced, and controlled the orientation of shear fractures. There was severe microcracking adjacent to these shear zones. For the fourth test, spalling was very intense and in the most deformed zones, two sets of fractures were developed, one pair parallel to the boundary of the opening and the other dipping inwards. Fractures which penetrated out from the spalled zone, tended to follow the bedding planes. In the fifth test, spalling extended for three to four millimeters into the rock. Radiating out from these zones were set cracks, which tended to be parallel to the bedding. These fractures coalesced to form a series of domical fractures.

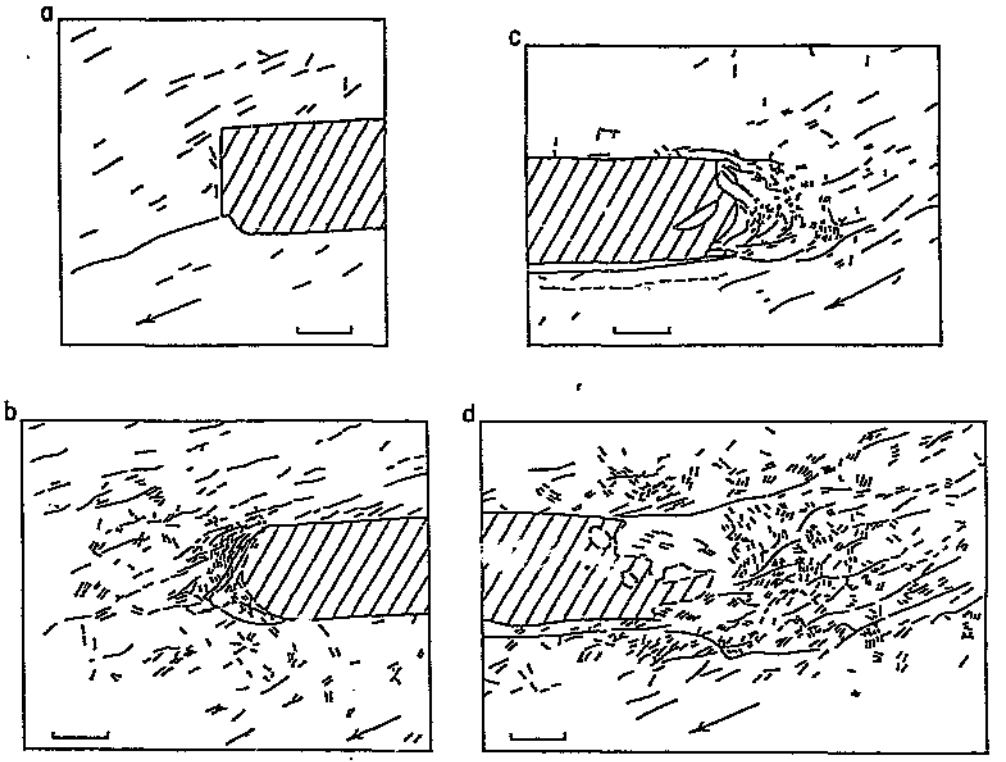


Figure 2.3.1. Fracture patterns around rectangular slits in quartzites, arrows parallel to bedding planes, scale bar represents 1mm. (N.C. Gay, 1972)

A strong lithological control of the development of fractures was found. The orientation of the shear zone was strongly controlled by bedding planes. Not all the fractures followed this direction. There was a dominant fracture which followed the boundary of the opening, and a smaller set of fractures which dipped in towards the slit. This was the first series of tests carried out by Gay (1972). These tests were all carried out on quartzite. Gay (1972) conducted a similar series of tests. These tests were carried out on sandstone. A brief look at these results are described. The results of these tests can be seen in Figure 2.3.2. Figure 2.3.2. (a), (b) and (d) are the results from tests 1, 2 and 3 respectively with increasing pressure being applied in each case. Figure 2.3.2. (c) shows a section perpendicular to the direction of excavating of the fifth test. Fracturing in the first test was confined to those grains adjacent to excavation. There was however a definite pattern with the majority of fracture following the outline of the slit and a couple of fracture dipping in towards the excavation. In the second test more intense fracturing was evident with fractures extended for more than one millimeter into the rock. Two sets of cracks are present, inward dipping and out-dipping. The inward-dipping microfractures being the more common fractures. The third test which can be seen by Figures 2.3.2. (c) and 2.3.2.(d), 2.3.2. (c) being a section perpendicular to the axis of the opening, the fracture zone extends four millimetres into the rock. Little fracturing along the length of the slit is evident. From figure 2.3.2.(d) inward dipping fractures are evident. Movement of the rock tended to be in the direction of the slit. Gay (1972) found that in this series of tests or rather in the sandstone samples, there was a complete absence of shear zones which cut into the rock.

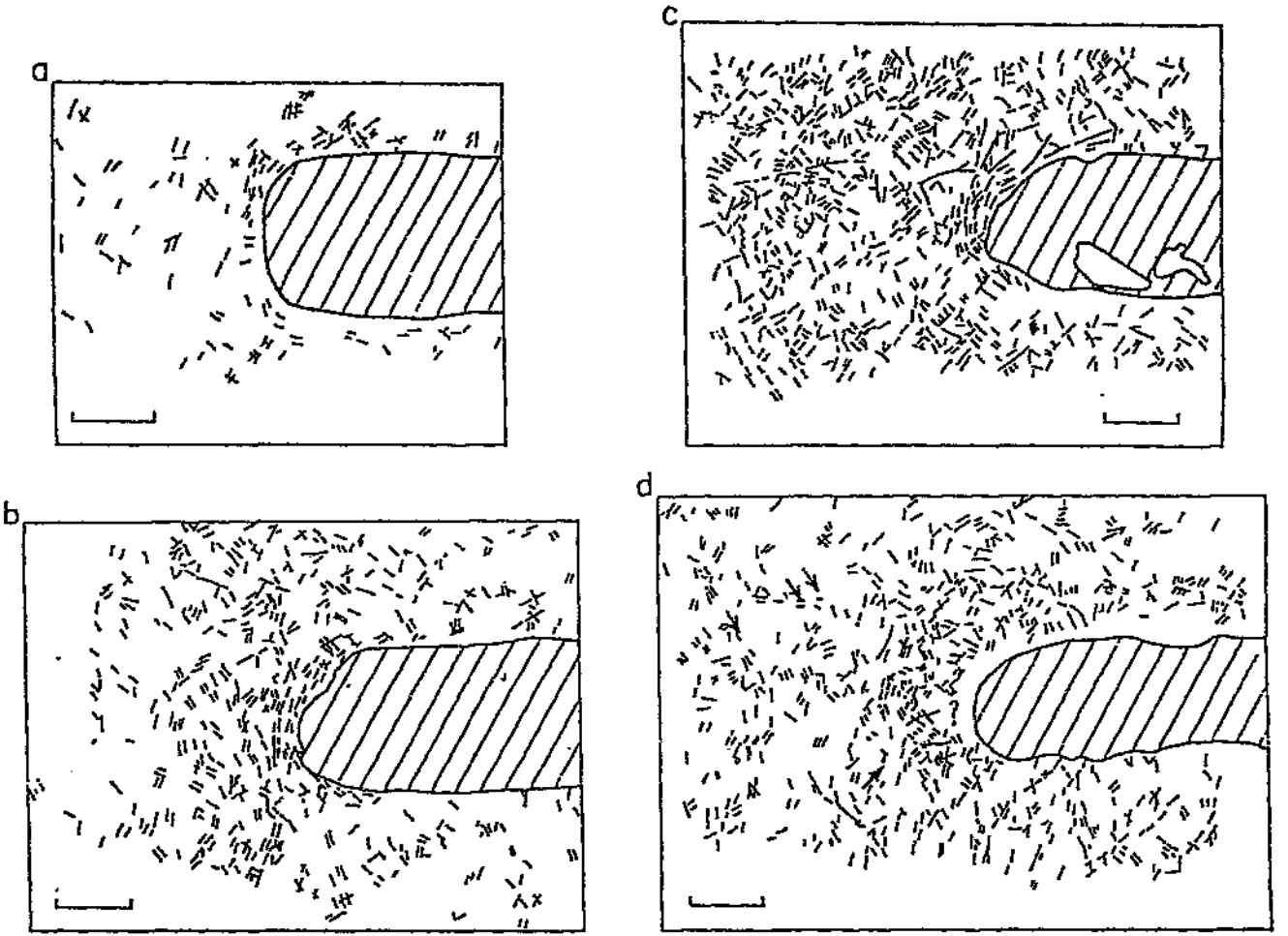


Figure 2.3.2. Fracture patterns around rectangular slits in sandstone, scale bars represents 1mm. (N.C. Gay, 1972)

Any major differences in the results given by Gay (1972) and results presented in this dissertation are going to mainly be due to the different stress conditions. In the tests done by Gay (1972), there is a hydrostatic stress condition, therefore the lack of a major principle stress direction. This condition does not exist in the underground situation, therefore the use of triaxial stress conditions to better simulate what happens underground. Fracture orientation underground has alot to do with the major principle stress direction. The lack of a major principle stress direction, as is the case with Gay (1972), would cause an inaccurate formation of the fracture zone. Ozbay and Ryder (1989) carried out pillar-stope tests under biaxial loading. Figure 2.3.3. shows the resulting fracture pattern. Tensile fractures marked 1 and 1A form near the

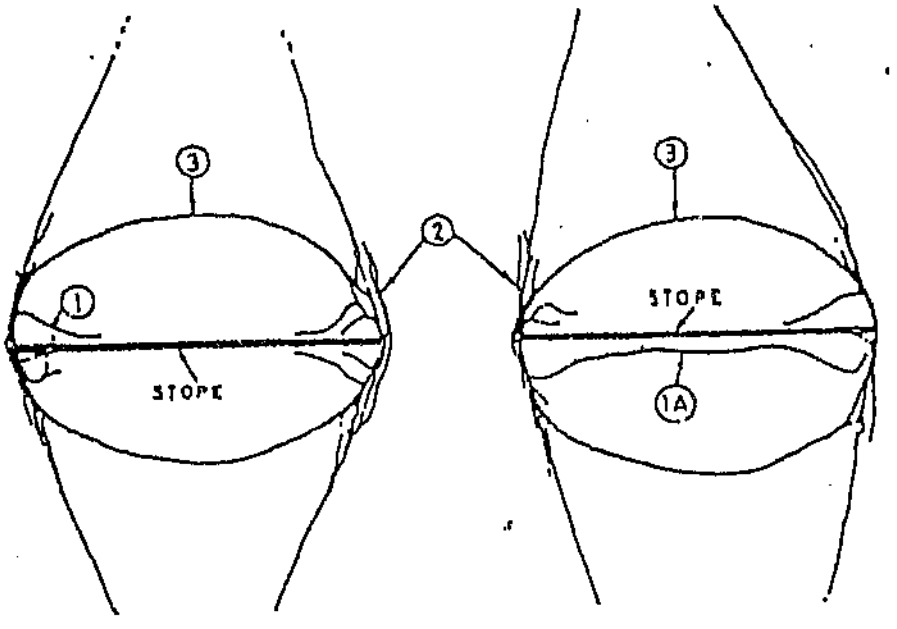


Figure 2.3.3. Schematic representation of the fracture pattern observed from the vertical sections taken from laboratory pillar-stope test specimens under biaxial loading conditions (Ozbay and Ryder, 1989)

edges of the pillars as well as macroshear fractures seen in the figure as 2. These shear fractures extend at angles of between 70 and 80 degrees over the simulated stope. The fractures marked 3 in figure 2.3.3. appear to be tensile in nature and form roughly elliptical arches over the openings. In both Ozbay and Ryder (1989) and Ozbay (1995), the tests differed from those presented in this dissertation in that the stress conditions are only biaxial. In this dissertation triaxial loading conditions are implemented. Also in the previous two experiments described above, no closure at the stope takes place, whereas in this dissertation , the stope is allowed to close totally. Ozbay (1995) carried out tests in the laboratory on the development of the fracture pattern on a deep level excavation. This excavation resembled that of a stope. Figure 2.3.4. shows the resulting fracture pattern from the tests carried out. Although not all the types of fractures as defined by Joughin and Jager (1984) are present, type 1 fractures or extension fractures are present. Ozbay also found that the growth of these fractures become more vertical as the opening is extended. This backs up Joughin and Jagers' theory that as the span of the stope increases so the steepness of the type 1 fractures take place.

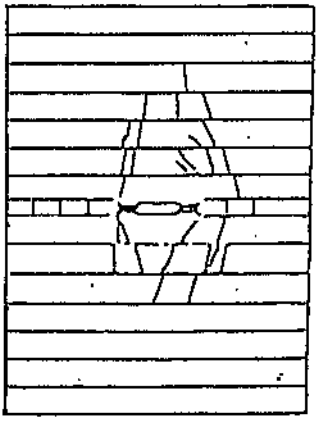


Figure 2.3.4. Schematic representation of the fracture pattern around a stope. (Ozbay, 1995)

2.4. Numerical Modeling

As is the case with the physical modelling, it is necessary to study simulations which have covered the same subject, or similar topics for the numerical case. The numerical case being the prediction of fracture patterns for a given geometry using a computer code.

Napier (1990) attempted to simulate the results of Ozbay and Ryders' (1989) experiments using the computer program called DIGS (Discontinuity Interaction and Growth Simulation). The results of these simulations can be seen in Figure 2.4.1. A close correlation between the experiments of Ozbay and Ryder (1989) and the numerical simulation can be seen . The tensile convex curvature fracture follow a very similar pattern to that of the physical experiments while the orientation of the shear fractures for the numerical simulation closely correlates to the results obtained in the laboratory. The type 1 fractures observed by Ozbay and Ryder (1989) in figure 2.3.3. were not simulated. Napier (1990) noted that the initial angle of propagation at the stope edge is a crucial parameter input if the correct fracture pattern is to be obtained. Napier also concluded that the simulation of underground stopes using numerical models depends critically on the mechanics of fracture initiation and propagation. Ozbay (1995) also did some fracture pattern simulation for the fracture patterns formed in figure 2.3.4. using DIGS. Tension fractures were specified, as the mode of failure in the physical tests were found to be tensile fractures. Figure 2.4.2. shows the simulated pattern of fracturing. Only the lower half is shown as the upper boundary was specified as a plane of symmetry.

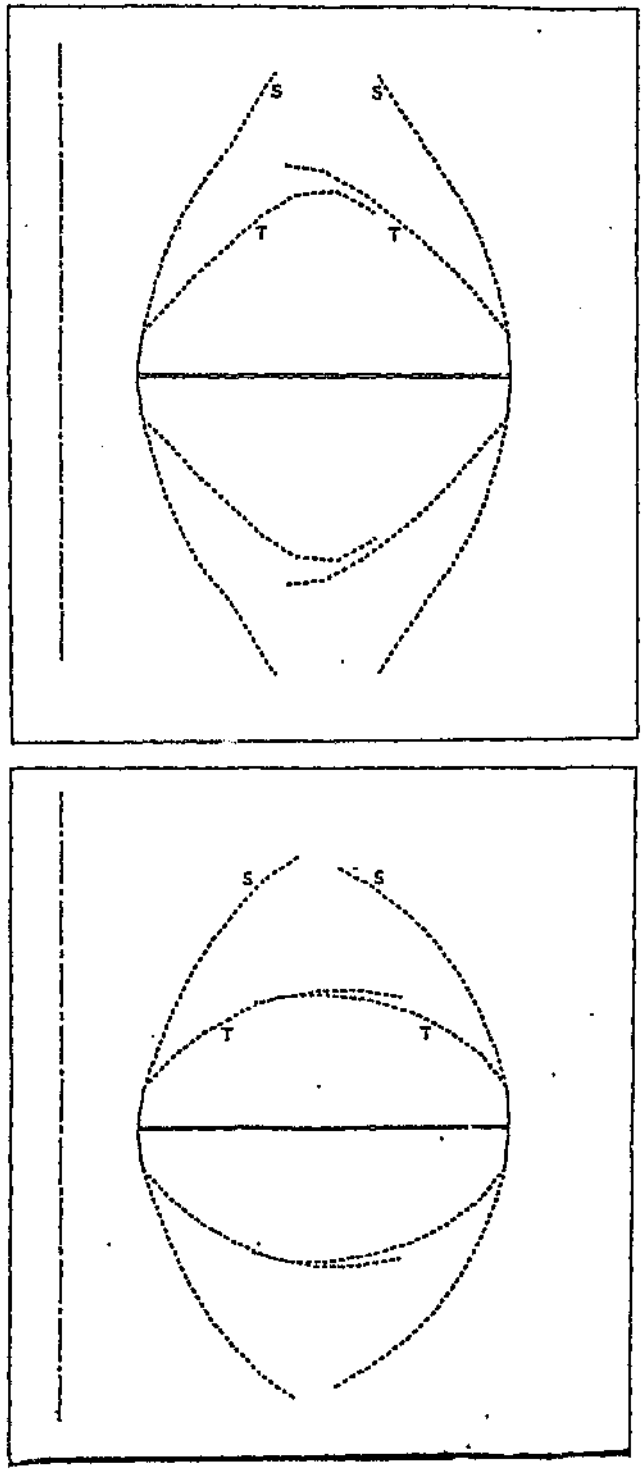


Figure 2.4.1. Numerical simulations of Ozbay and Ryders' experiments using DIGS (Napier, 1990)

Tensile stresses induced parallel to the horizontal surface of the opening caused the formation of tensile fractures at the centre of the opening. As discrepancy between the physical experiments and numerical simulations was observed as these tensile fractures found at the centre of the opening of the stop, in the numerical simulations did not form in the physical experiment.

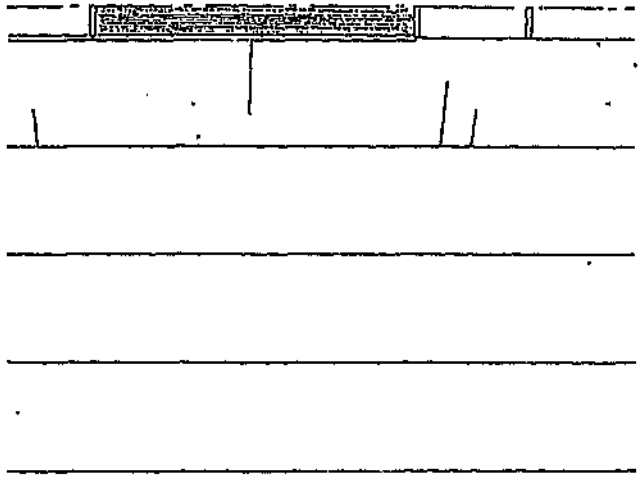


Figure 2.4.2. Simulating fracture growth using tensile fracture growth rule (Ozbay, 1995)

Ozbay carried out the same simulation using DIGS, except this time the fractures were only allowed to grow in shear. The resulting fracture pattern can be seen in figure 2.4.3. which shows a significant alteration in the final fracture pattern. None of the tensile fracture formed at the centre of the opening as was the case in the previous simulation.

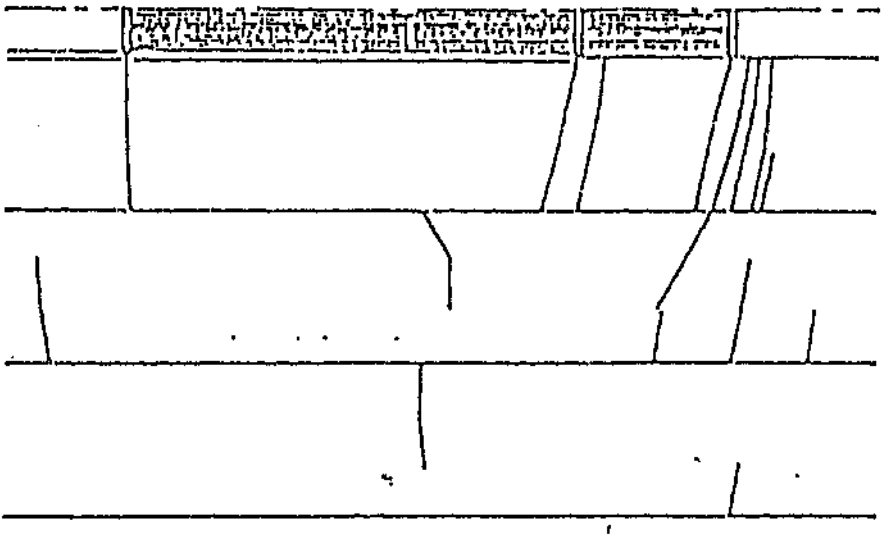


Figure 2.4.3. Simulating fracture growth using the shear fracture growth rule (Ozbay, 1995).

Sellers (1997) did some simulations of the fracture zone around a stope using DIGS, the tesselation version. The tesselation being a grid of pre-defined possible fracture sites defined using a triangulation procedure. The mechanism for determining failure or no failure still remains the same. The results of Seller's simulations can be seen in Figures 2.4.4., 2.4.5., 2.4.6.and 2.4.7 In Figure 2.4.4., Seller's simulated 14 mining steps of one millimeter in a uniform rockmass. Sellers (1997) found that the zone of activated fractures increased as the excavation progressed as is found in an underground situation. The majority of the fractures around the stope face dip at steep angles towards the face in a hangingwall and away from the face in the footwall. As the stope extends forward, so the existing fractures formed previously, now behind the

stope face, also extend. The dips of these fractures decreases as the distance of these fractures from the face increases. Sellers' simulations formed a fracture zone front, the equivalent of about 1 metre ahead of the face and extended behind the stope following the arching of the compressive principle stress.

The influence of bedding planes or parting planes were also simulated using the DIGS tesselation approach. The friction angle of the parting planes were varied. Sellers (1997) used a relatively large friction angle of 30 degrees for both un-mobilised and mobilised cases. Figure 2.4.5. shows the result of this simulation with the fracture zone extending behind the stope face. It was found that slip on the parting plane only occur above and below the excavated region. The orientation of the active fracture tend to be in the vertical direction. The fract es are continuous across the parting plane. A test with a lower un-mobilised friction angle of 5 degrees and mobilised friction of 4 degrees was used. This has the effect of causing the parting planes to be activated ahead of the stope. Fractures form of the surface of the parting plane closest to the stope as can be seen in figure 2.4.6. The rock in between the parting planes acts as a set of cantilevered beams. These beams fail in tension at the point of slip, while the remaining beam is clamped ahead of the face.

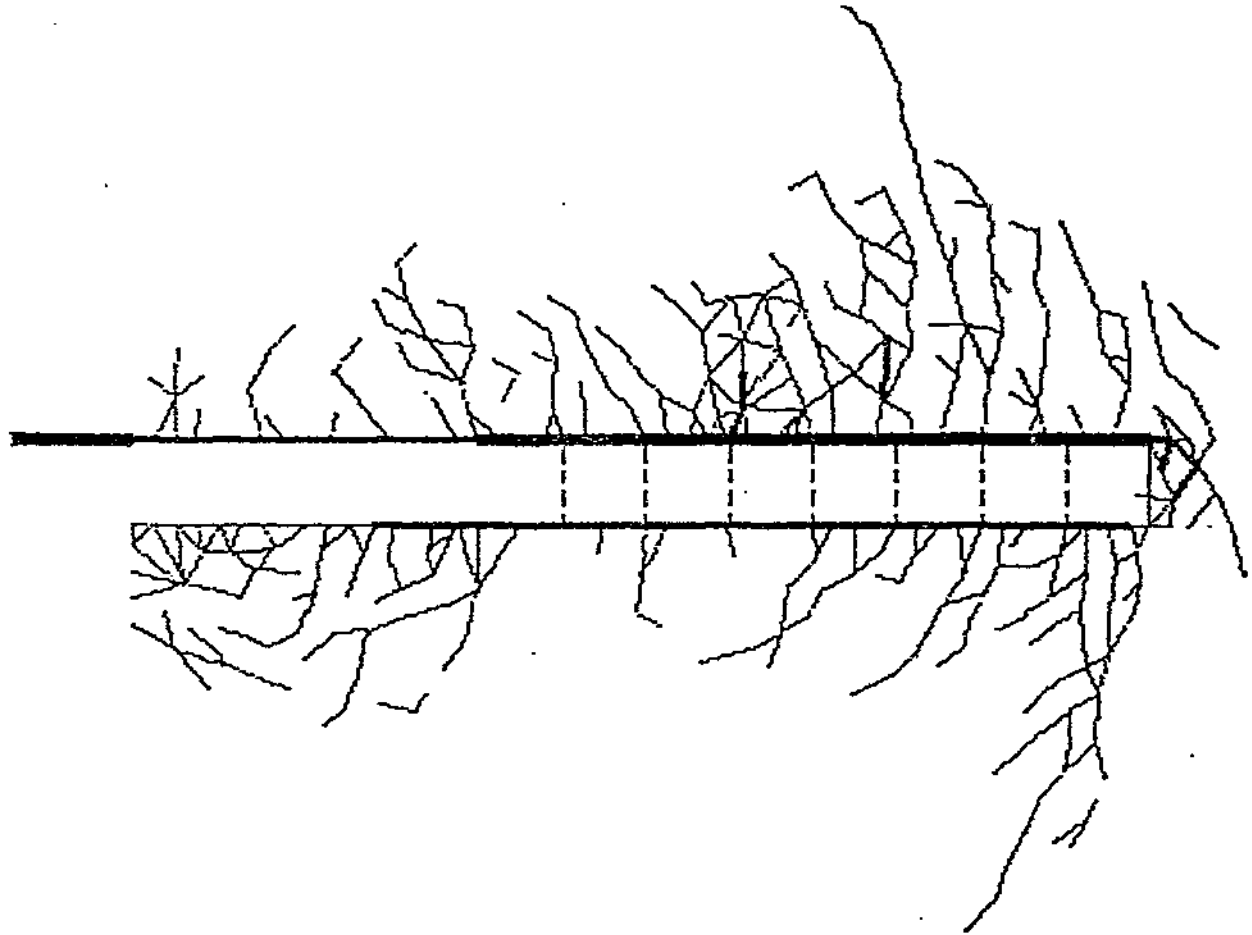


Figure 2.4.4. Fracture pattern after 14 mining steps of 1m in a uniform rockmass (Sellers, 1997)

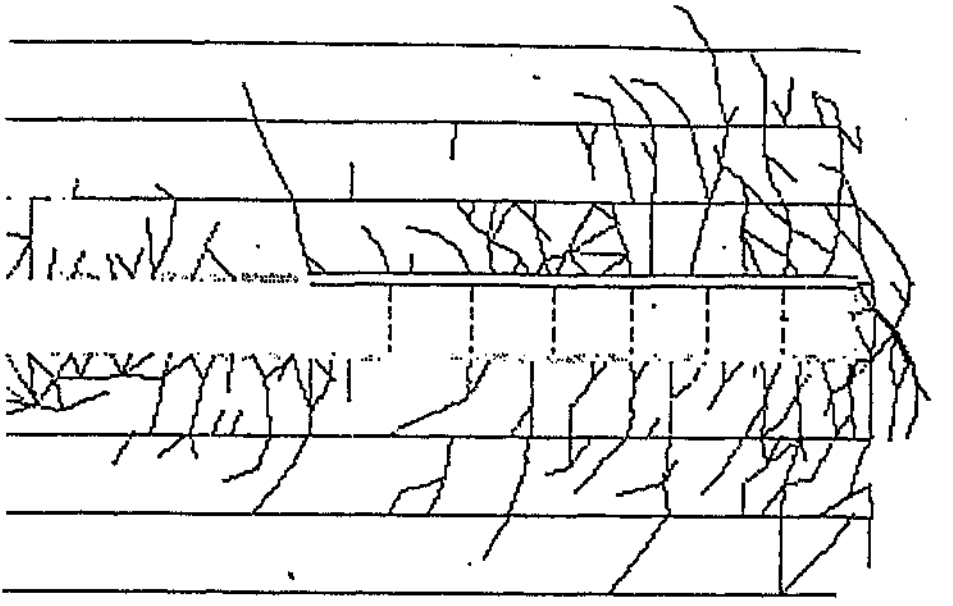


Figure 2.4.5. The effect of parting planes on the fracture pattern around a stope with high friction angles (Sellers, 1997)

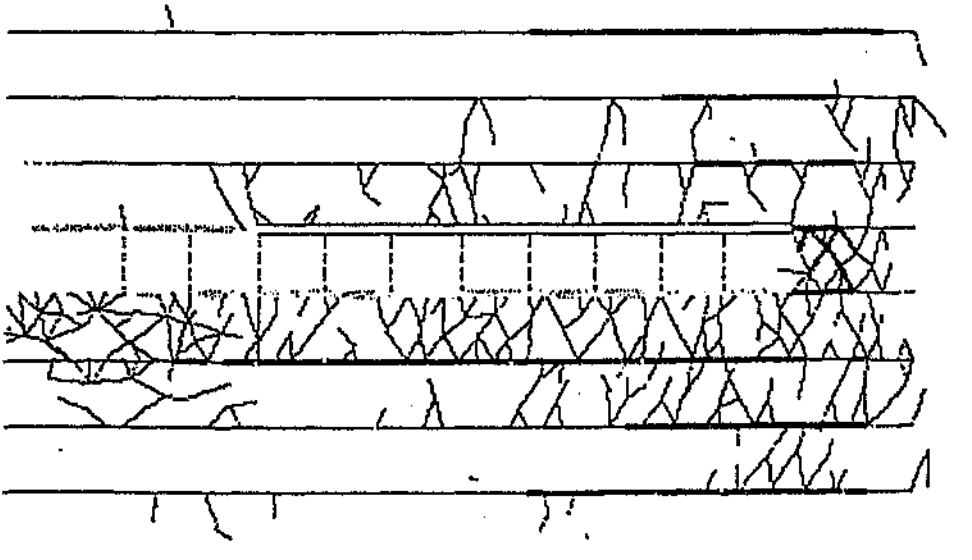


Figure 2.4.6. The effect of parting planes on the fracture pattern around a stope with low friction angles (Sellers, 1997).

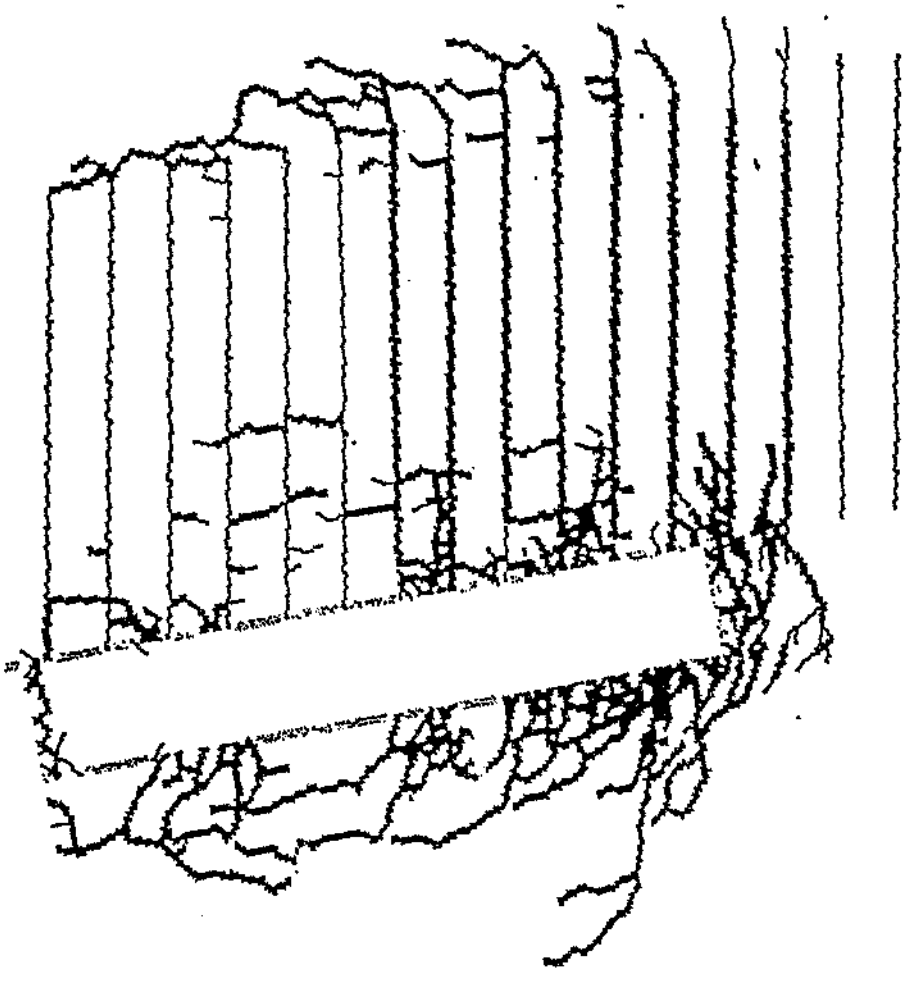


Figure 2.4.7. Fracture initiation in a stope with a set of steeply dipping joints i

hangingwall (Sellers, 1997)

The effect of a pre-existing joint set on the fracture zone around the stope was also simulated using the tesselation approach. Sellers (1997) chose to simulate joints in the hangingwall which dipped at 80 degrees away form the face. The result can be seen in Figure 2.4.7. As mining progressed, failure by sliding of the joints occurred slightly ahead of the face sub-parallel to the joints, fracturing formed ahead of the face which extended into the hangingwall. Due to the movement of the joints into the mined out area, horizontal fractures form both above and within the jointed zone.

The objective of this literature survey is to give the reader an idea of the fracture zone around a deep level stope. To give the reader an idea of what causes the fractures as well as what determines the direction in which the fractures form, along with the mode of fracturing that occurs, be it either tensile fracturing or shear fracturing, or a combination of the two. The effect of what happens once the fractures have been formed is also important to understand, with regards the supporting of the hangingwall. This survey has briefly looked at the worked carried out in the field of the numerical simulation of the fracture patterns around a deep level stope taking into account the effect that geological structures may have on the final fracture pattern. The purpose of the literature survey is also to have a reference which the results of this dissertation can either agree or disagree with authors of previous published results.

III Failure in Brittle Rock

Determining whether brittle rock fractures is an important factor, for obvious reasons. Research into the area of rock fracturing has been carried out. The Mohr-Coulomb failure criterion is the most commonly used failure criterion in determining whether a rock will fail or not. The numerical code DIGS also uses this criterion to determine the failure of rock. Figure 3.1 shows a general Mohr-Coulomb envelope for a specific rock type. The diagram shows two Mohr-Coulomb envelopes, the upper envelope showing the static stress envelope while the lower line indicating the dynamic stress envelope. Static being the envelope of reference while the rock is still intact for determining failure, while the dynamic envelope being referred to once the rock has failed to determine whether slip will take place. On the vertical axis is τ, which is the shear stress and σ_n on the horizontal axis which is the normal stress.

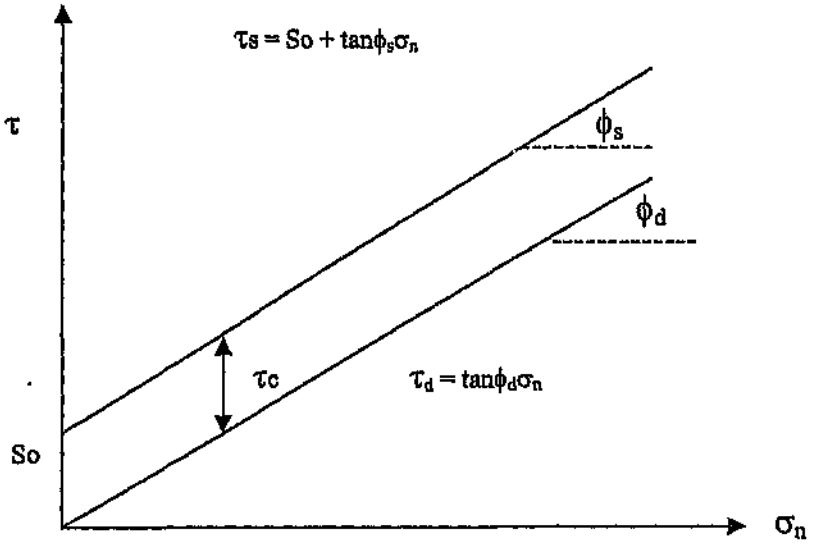


Figure 3.1. General Mohr-Coulomb envelope for a rock type.

τ_s – Static shear stress

σ_n – Normal Stress

ϕ_s – Static friction angle

ϕ_d – Dynamic friction angle

S_o – Cohesion

To determine whether failure will occur or not, the stress conditions of a point are plotted on the same set of axes as the Mohr-coulomb envelope. If this point is below the Mohr-coulomb envelope, failure will not occur. If, on the other hand, the point is above the Mohr-Coulomb envelope, failure of the rock should then take place. Once the rock has failed and it is necessary to determine if slip or movement is going to take place, the lower graph in Figure 3.1 is used. The approximate difference between the top graph and the bottom graph is the cohesion. Once rock has failed it has very little or no cohesion. The friction angle also changes and is usually slightly less for the mobilised case than for the un-mobilised case. The stress conditions, namely the shear stress and normal stress are now plotted for the failed zone. If this point exceeds the graph for the mobilised or dynamic case, slip is likely to take place. If the point is below the graph for the dynamic case, then slip is not likely to take place.

The numerical code DIGS used to simulate fracture growth is this dissertation uses this Mohr-Coulomb failure criterion with a few modifications added to it. DIGS is two dimensional and hence represents its fractures in a plane stress or strain geometry's by joining linear segments end to end. Each of these segments is

characterized by a displacement discontinuity density. The displacement discontinuity is assumed to vary linearly along each element. Stress or displacement boundary conditions are matched at two collocation points within each linear variation element. This serves to eliminate the over estimation of the displacement discontinuity magnitudes which is caused when the constant strength elements are used.

Controlling fracture growth is by evaluating the stress field round a set of potential growth sites. Theses sites consist of either seed points at selected positions in the geometry being simulated or at the joining point between existing elements or at the tips of growing fracture segments. In the case of a free standing seed point, a measure of the possibility for fracture initiation is determined from the stress conditions at that point.

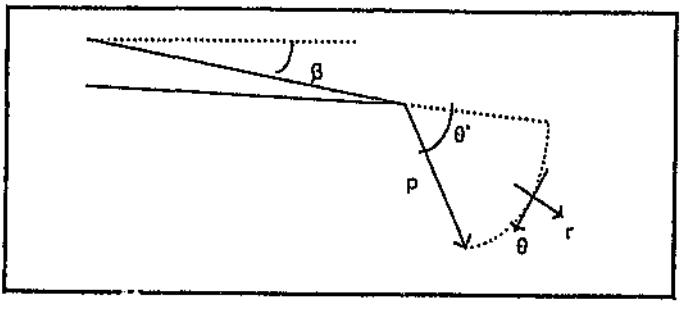


Figure 3.2. Selection of crack growth angle from an existing crack tip, T, by direct evaluation of the stress field at point P a fixed radius ρ from T (Napier, 1990, Napier and Hilyard, 1992)

For extension or tensile fracture, growth is the magnitude of the most tensile principal stress component. If the orientation of this component is at angle α with respect to a specified global co-ordinate system it is assumed that the fracture grow in either the direction $\alpha_1 = \alpha + \pi/2$ or $\alpha_2 = \alpha - \pi/2$. To determine the direction of growth, a base angle β which is an input value and associated with each seed point and the angle α_1 and α_2. The closest angle of α_1 and α_2 to the angle β is chosen as the growth direction. To avoid engineering the direction of growth of a fracture of several seed points, β can be set to a random angle for each point and two complementary seeds with angle β and $\beta + \pi$ can be specified at each point. (Napier and Hildyard, 1992)

In the case of an already existing and growing fracture, determining the direction of growth of whether growth of the fracture will continues is a more complicated matter. The base angle, β, is assumed to be the angle of the previous element in the segment. (Figure 3.2). The optimum growth angle is found by a direct search of the stress conditions at a given fixed radius ρ from the crack tip. The length of this radius is the length of an element for the given simulation. In the case of extension fracture growth, the optimum angle θ^* is the position ρ at which $\tau_{\theta\theta}$ is a maximum. Tensile tresses are assumed to be positive. The tendency for tensile fracture to grow in the search method is measured by the maximum magnitude $\tau^*_{\theta\theta} = \tau_{\theta\theta}(\theta^*)$. The potential growth site, be it the seed point or an existing crack tip, is found by searching for the maximum of the minor principal stress or $\tau^*_{\theta\theta}$ at all possible growth sites. A single element is then introduced at the most favourable site in the correct direction. The entire problem is then solved again with the new element included. The search procedure is then repeated using the end point of the new element as a starting point to search for a new possible crack. This procedure ends when the element the

element that would be introduced at the most favourable position for the crack to grow would not b- .nobilised according to the defined Mohr-Coulomb failure criterion. The Mohr-Coulomb criterion is defined by a linear relationship of the form.

$$\sigma_1 = -\sigma_c + m\sigma_3$$

where

σ_c = Uniaxial Compressive Strength

σ_3 = Minor principle stress component

σ_1 = Major principle stress component

For a negative compressive stress convention, $\sigma_t < \sigma_3$. Another tension cutoff parameter, τc, can be specified to limit the maximum tensile strength of the material. Shear failure is a more complex process than the extension growth of a fracture. Shear failure is simulated using the same seed and crack growth criterion previously described for extension fracturing, but a different rule for determining the angle and possibility for fracture initiation and growth is used. The shear growth direction is determined by finding the angle of which the local strain energy release is a maximum (Napier et. al., 1995). Energy release rate being the quantity of energy which is theoretically rel[illegible] in the course of enlarging an excavation (Legge, 1986). That is, finding the maxim[illegible]ue of

$$G = (\tau^2_{r\theta} - \mu\tau_{\theta\theta}^2)$$

where r = direction of proposed element.

θ = direction normal to the proposed element.

μ = effective friction coefficient.

$\tau_{r\theta}$ = sheer stress on element.

$\tau_{\theta\theta}$ = normal stress across element.

In setting up the problem in DIGS, sheer fracture seeds need to be distinguished from tensile fracture seeds. Each seed point must have a reference to a constitutive definition in which the failure properties of the material are specified in terms of the Mohr-Colomb parameters, namely σ_3, m and τc. Once the crack element is put into position at the defined seed point, a specified mobilised friction angle and cohesion is applied to the crack element. Some judgment needs to be exercised by the modeler about the selection of the shear or tension fracture growth mode and in certain cases simulations must be restricted to only one node. (Napier, 1990)

One of DIGS' major disadvantages is the fact that the positioning of seed points is necessary before running a simulation. In order for this to be done successfully, prior knowledge is necessary to determine the possibility of failure at a specific point in the geometry, relative to other points in the given geometry. Failure to define the correct positioning of the seed points will lead to incorrect fracture pattern formations.

DIGS is a two-dimensional simulation program. DIGS assumes an infinite third dimension, this translates into an equal stress along the entire and infinite third dimension. This means that the fracture patterns in the third dimension for each case will be identical, therefore in this version of DIGS, the third dimension becomes irrelevant.

Some parameters which needs to be input into DIGS may be unclear. Mobilised cohesion refers to the case where the material has failed, any further analysis in-terms of further fracture propagation will make use of the dynamic Mohr-Coulomb model. While an un-mobilised cohesion situation refers to the case of a material which has not fractured. Any analysis of this situation in terms of failure will make use of the static Mohr-Coulomb envelope.

DIGS is the numerical code used to simulate fracture patterns in this dissertation. Other codes which could have been chosen are ELPHEN which is a finite element code and WAVE which is a finite difference code. The reason DIGS was used is because it is a boundary element code. The following brief discussion will outline the major differences between the different codes.

WAVE is a finite difference program. All the numerical codes use the rule that the external energy, in other words the stress applied to the boundaries of the specified geometry, must equal the internal energy. The meaning of the finite difference is that at any time during a simulation using WAVE the external energy will not equal the internal energy, however the difference will be defined number, ie it will not be finite. The reason that the external energy will not equal the internal energy is because WAVE uses a leap-frog method where new stresses are calculated from velocities and velocities are calculated from stresses. WAVE uses a staggered mesh to solve for stresses and velocities of different positions. WAVE is however known for its efficiency. Its efficiency is accuracy, speed and use of computer memory. This efficiency is partially due to the staggered mesh as fewer grid points are necessary for the same accuracy. Either the stress of velocity for each element needs to be

calculated. Each element needs to be a whole element and not split up. It is for this reason that WAVE can not accommodate oblique discontinuities (Sellers, personal interview, 1997). It follows that WAVE would not be a suitable method code to use in the simulations which follow in this dissertation.

ELPHEN, the finite element code, was also an option, but has disadvantages. As in the case for WAVE, the external energy applied to the geometry must equal the total of the sum of the energies of all the small elements. Energy is equal to the produce of the traction and the displacement. Traction is equal to the product of the stress and the area of each element. An element in a geometry defined in ELPHEN will influence the elements surrounding it applying a traction, and a displacement. The product of these two giving the energy in the element. A defined geometry will contain a defined number of elements, hence the name of the finite element code. However if failure localises into narrow regions, for example shear bands, spatial grid systems can impose cumbersome restrictions on the movement of material. Once failure has occurred many of the continuum constitutive assumptions may be violated. An example of these assumptions being that that material properties remain the same isotropic and that the principal stress and principal strain share a common axis (Sellers, personal interview, 1997). For this reason ELPHEN was not chosen as the numerical model to carry out numerical simulation.

DIGS is a boundary element code. In the same way as the two numerical simulation mentioned above so in DIGS the same formulae applies. The formulae that the external energy must equal the sum of the individual internal elements. DIGS differs from the previous two models in that it doesn't divide the given geometry into

smaller two dimensional blocks, but rather it divides the boundaries into smaller elements. If these boundary elements move due to certain criterion, a displacement discontinuity is formed. The energy for each is then the product of the traction and the displacement discontinuity of each element. As a crack grows, so more elements are added to the problem in the form of a boundary. Benchmarks are defined by the modeler to determine the stress conditions at other points within the geometry apart from the boundary elements. Each benchmark will be influenced by each boundary element. This influence is defined by the modeler and is a function of the distance that the boundary element is from the benchmark and becomes the influence coefficient (Sellers, personal interview, 1997). The stress conditions for each benchmark can then be calculated. DIGS can accommodate various geometry's as well as oblique fractures and discontinuities and was therefore chosen to simulate the fracture patterns obtained in the physical models.

IV Experimental Setup

The previous physical experiments carried out that were described in the literature survey where either carried out on circular samples with hydrostatic pressure being applied to the sample, or the samples were rectangular samples with only two dimensions of stress being applied to the sample. For this reason, a biaxial load cell was developed. The cell provides the confining pressure and an LVDT controlled MTS machine provides the vertical load. Using this equipment it is possible to provide triaxial loading conditions to the samples.

4.1 The biaxial load cell

The biaxial load cell is constructed from a steel ring with dimensions of 360 mm outer diameter, 160 mm inner diameter and 120 mm height (Figure 4.1). The lateral confining stresses are provided by the two hydraulic pistons built into the ring. Curved spacers are used to convert inner sides to squares to accommodate cubic specimens. Additional prismatic spacers can be used to change the inner dimensions of the cell to accommodate different sizes of specimens, typically cubes with 70, 80, and 100 mm side lengths. The coefficient of friction of rock-steel contact is reduced to 0,001 by applying stearic acid on all six sides of the specimen.

A centrifugal electric pump delivers hydraulic pressure to the two hydraulic pistons, which in turn apply the pressure onto the specimen. The maximum load that can be applied on the specimen is about 170 KN, which is equivalent to a lateral confinement magnitude of 27 MPa on the side of an 80 mm cube block. The electronic gauge, which is placed between the cell and a needle valve mounted on the hydraulic fluid

pipe, measures the pressure being delivered to each hydraulic piston. A pair of dial gauges is also mounted on the fluid pipe for visually observing the pressure. T o needle valves are placed before the gauges to lock the pressure at a desired level.

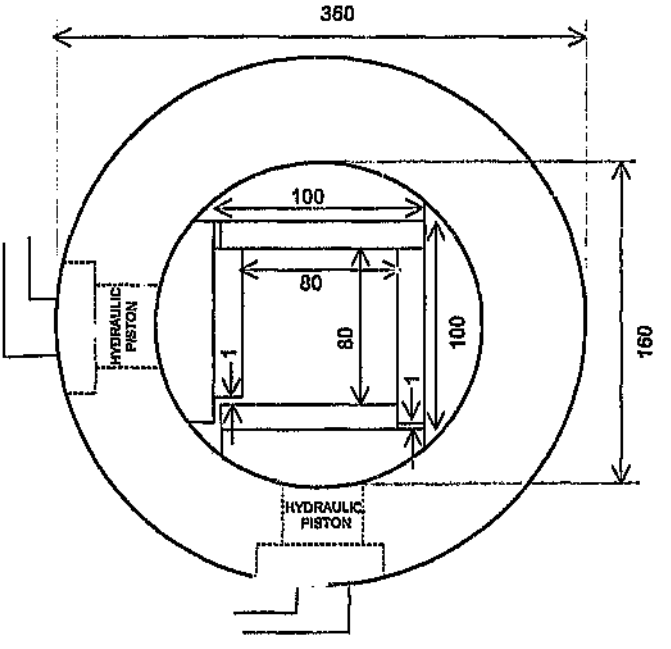


Figure 4.1 A schematic of the biaxial cell used for the experiments (dimensions are in mm).

The 2800 KN actuator piston of the MTS 815 compression testing machine is used to apply a vertical load on the specimen. The built-in LVDT measures the piston displacement. The vertical loading of the specimen is programmed on the MTS TestStar software which runs on an OS/2-based computer.

4.2 Specimens

The models were prepared from Elsburg Quartzite, Black Reef Quartzite and Norite. The properties of the rock types used for making the test samples are given in Table 1.

Table 1 Material properties of the rock types used for the experiments.

	Elsburg Quartzite	Black Reef Quartzite	Norite
Uniaxial Compressive strength	180 MPa	203 MPa	290 MPa
Elastic modulus	69,6 GPa	78 GPa	90 GPa
Poisson's ratio	0,20	0,17	0,28
p-wave velocity	5200 m/s	5500 m/s	

The models are typically cubic blocks with a side length of 80 mm. All sides are machined perpendicular to within 0.01°. The block is cut into two 80x80x40 mm prismatic blocks and one of them is machined to create a horizontal "stope" when put under the solid block. Figure 4.2 shows a typical specimen geometry used for the experiments.

4.3 Data acquisition

The vertical displacement of the actuator piston and load applied are recorded by the MTS data acquisition system. An external data acquisition system is also used to record the vertical load from a load cell placed on the top platen, the pressure measured by electronic pressure gauges, and the horizontal displacements measured by cantilever gauges. During the initial tests some problems were encountered leading to the loss of some information.

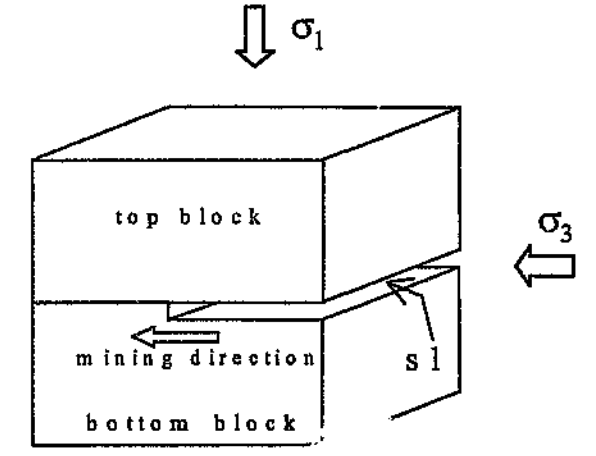


Figure 4.2 A typical test specimen geometry.

The horizontal displacements being measured by the cantilever were not mounted perpendicularly to the sample due to development calculations leading to invalid results. Another problem discovered some time later caused by frequent transportation of the equipment was the presence of a potential difference across the cantilever leading to erroneous results. These problems were sorted out, however, much horizontal displacement information was lost due to the incorrect readings being recorded.

An acoustic emission system, which operates at a data acquisition rate of 4 MHz per channel, was used to record the location of fracturing. Three-dimensional location of fracturing was achieved using 9 sensors positioned around the sample in the slots machined into the side platens. A one millimetre thick steel membrane separates the sensors from the specimen. The location calculations were done using the least squares algorithm.

4.4 Testing procedure

The testing takes place in a standard sequence: The MTS actuator piston applies the principal stress for the experiments. Two independent confining stresses are applied via pistons embedded in the biaxial cell. A centrifugal pump drives the pistons and the pressure is controlled manually using the two needle valves. The sample is initially confined triaxially to a pressure of 27 MPa. Once this is achieved, the valves on the cell are closed which means that the confinement will increase as the sample deforms in the horizontal direction. Vertical loading continues at a rate of 0.005 mm/sec until a vertical pressure of 80 MPa is reached. This state of stress is held for approximately 5 minutes after which the vertical stress is reduced slowly to 27 MPa. Then both vertical and horizontal stresses are reduced to zero. The specimen is taken out of the cell and the stope is extended in length by 1mm and the process is repeated.

Analysis of Tests

A total of about 25 laboratory tests and their corresponding modelling with DIGS were carried out. The tests can be grouped under four major categories:

- Effect of closure
- Mining steps in a solid block
- Mining steps with a natural discontinuity
- Mining steps with cut parting planes

A summary of the types of tests conducted is presented in Table 1 and the relevant descriptions and discussion of the tests and corresponding modelling studies are given below.

V Analysis of fracture formation during Elastic Closure

This series was carried out to observe the effect of closure on the fracture patterns occurring around the face area of a stope. Three tests were carried out on specimens having stoping widths of 0,2, 2, and 3 mm.

The specimen with 0,2 mm stope width was loaded to 384 MPa and a total closure in the stope up to 7 mm from the face was observed in this case. For the cases of 2 and 3 mm stope width, no total closure was observed. Similar results were obtained from numerical modelling in that the 0,2 mm stope closed up to 7 mm from the face, while no total closure occurred in 2 and 3 mm stope width models as shown in Figure 5.1. Based on these observations, the stoping width was kept at 0,5 mm to ensure that closure occurs in the stope for the remaining experiments.

Table 1 Summary of the types of tests conducted.

Step, Specimen, stoping width (mm)	Vertical Load (MPa)	Confinement (MPa)		Closure from face (mm)		Stress/Strain ratio at maximum load (GPa)
		Initial	Final	Lab. Test	Num mod.	
Effect of Closure						
1, EQ, 0,2	384	27,00		7	7,58	35
1, EQ, 2,0	160	27,00		None	None	16
1, EQ, 3,0	115	27,00		None	None	17
Mining steps in a solid block						
1, EQ, 0,5	261	27,00		14	8	27
2, EQ, 0,5	260	27,00		14	9	26
3, EQ, 0,5	262	27,00		15	7	24
4, EQ, 0,5	257	27,00		16	7	23
5, EQ, 0,5	264	27,00		14	8	22,5
6, EQ, 0,5	267	27,00		14	9	23,2
7, EQ, 0,5	260	27,00		14	9	22
Mining steps with a natural discontinuity						
1, EQ, 0,5	100	27,00		22	12	32
2, EQ, 0,5	80	27.00	28.13	23	13	30
3, EQ, 0,5	80	27.65	28.28	23	11	30

4, EQ, 0,5	80	27.60	28.30	24	12	19
5, EQ, 0,5	80	27.68	28.40	25	13	17
6, EQ, 0,5	80	27.16	27.81	23	13	16
7, EQ, 0,5	80	27,00		25	14	15
8, EQ, 0,5	80	25.87	28.14	22	15	15,5
9, EQ, 0,5	80	27.49	28.24	22	15	14.6
10, EQ, 0,5	80	27		24		15
Mining steps with cut parting planes						
1,BRQ, 2x0.25	80	27.16	27.05	None	8	17
2,BRQ, 2x0.25	100	27.32	27.22	None	9	30
3,BRQ, 2x0.25	100	26.78	26.68	None	9	19
4,BRQ, 2x0.25	100	28.08	27.49	None	8	20
5,BRQ, 2x0.25	120	26.46	25.81	None	9	22

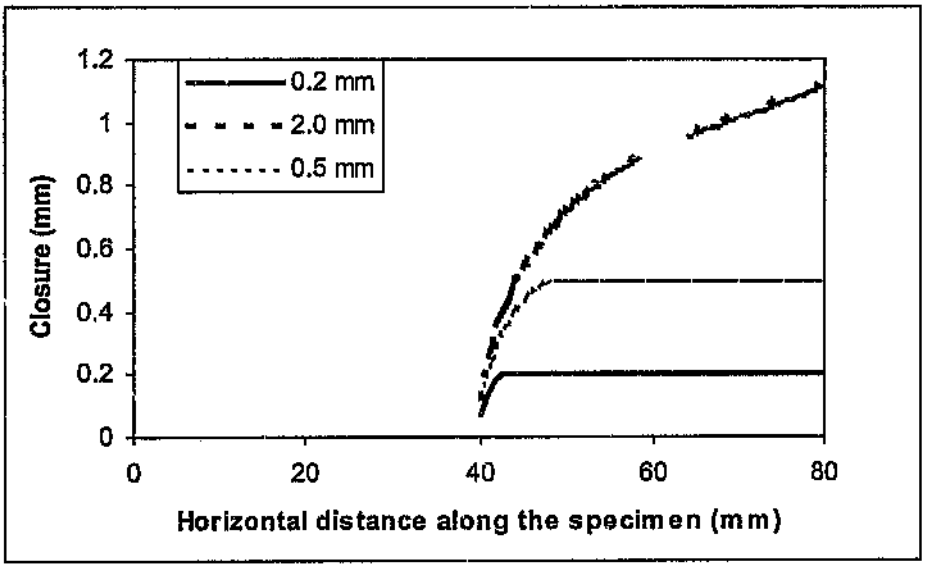


Figure 5.1. Graph showing closure profiles for stoping widths of 0.2mm, 0.5mm and 2mm

The fracture patterns observed from testing and modeling are compared in Figure 5.2. As seen, the tests with total closure result in fractures forming away from the stope. In the case of no total closure occurring, the fracturing is inclined towards the stope. The fracture patterns produced by DIG.. were observed to be dependent on the location of seed points and the failure criterion used. The fracturing resulting from

the extension failure criterion tends to develop towards the stope while fractures occurred in shear develop away from the stope. Closure in the stope limits the extent of extension fracturing and also causes shallower angle shear fractures than the no closure case. The results shown for the case of no closure are similar to those results obtained by Ozbay and Ryder (1989). The domical extension fractures extending above and below the machined out area. In this experiment it was found that both tension and shear cracks propagate from the nucleating edge as can be seen in figure 5.2., the top left photograph. In comparing the DIGS shear failure criterion output figure 5.2. The case for no closure, or the output on the left, domical shear fractures are formed behind the face both in the hangingwall and the footwall. For the case of closure, the shear fracture still forms ahead of the face, however the elliptical shape is eliminated and rather a constant almost linear fracture is formed. Comparing the outputs from the physical model and the numerical simulations shows that the simulation for the closure case is a better representation of the physical experiments fracture pattern. The DIGS shear fracture for the numerical simulation is less steep compared to the physical experiment.

The results of Gay (1976) bear a resemblance to those obtained in this experiment where no closure occurs. Figure 2.3.1 shows the output obtained by Gay (1976) with a σ_h/σ_v ratio of 0.5. The same ratio for the experiment in figure 5.2. gave a value of 0.34. Gay (1976) carried out the same test except under uniaxial compressive conditions. The results can be seen in figure 2.3.2 The elliptical shaped tension fractures are no longer evident as was the case under triaxial conditions. The tension fractures form in a linear fashion at steep angles in the direction of the stope. These results for Gay (1976) for the uniaxial loading conditions are similar to those obtained

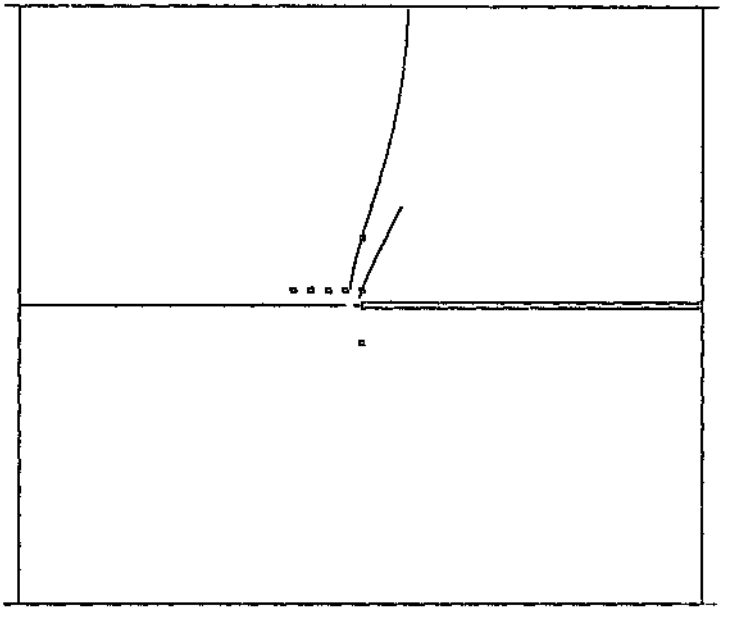
for the numerical simulation using the extension failure criterion for no closure of the stope in figure 5.2. This suggests that if in the physical case when the σ_h/σ_v ratio is about 0.34 elliptical tensile fractures are formed , while the results from the numerical case resemble a σ_h/σ_v ratio of zero in the physical experiments, then the horizontal influence co-efficient may not be adequate enough to cause the elliptical fractures.



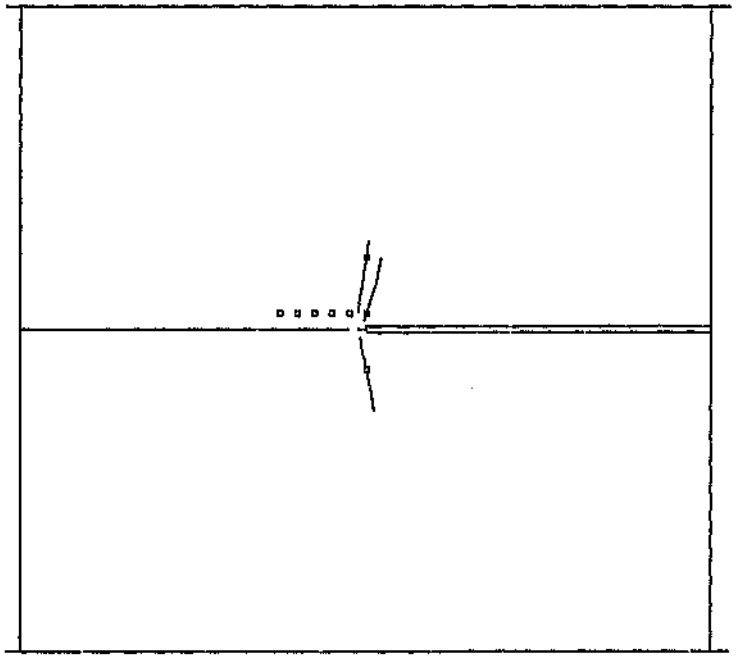


Experimental results

Figure 5.2 The fracture patterns observed from testing and modeling



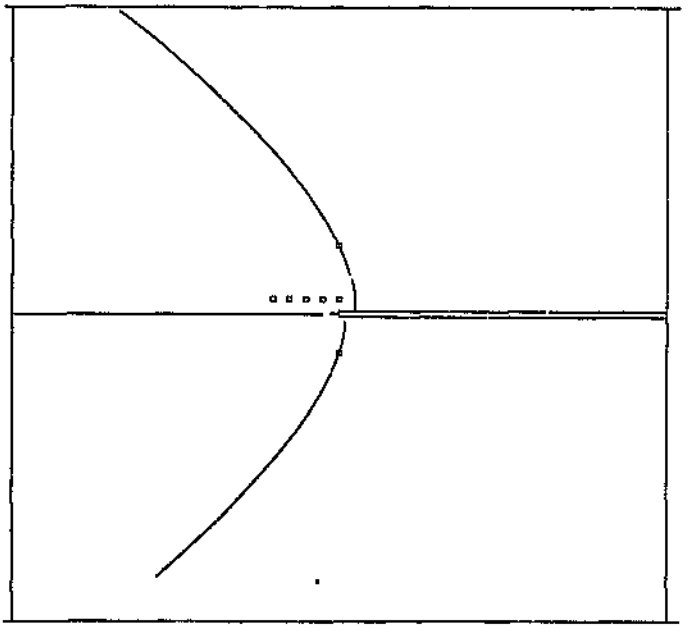
No Closure



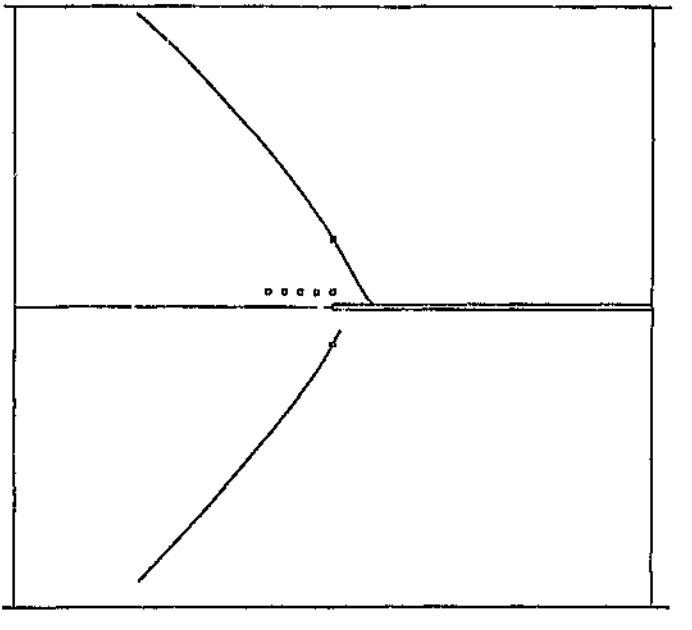
Closure

DIGS – Extension failure criterion

Figure 5.2 The fracture patterns observed from testing and modeling



No Closure



Closure

DIGS – Shear failure criterion

Figure 5.2 The fracture patterns observed from testing and modeling

5.1.1 Stress strain data for the case of no closure.

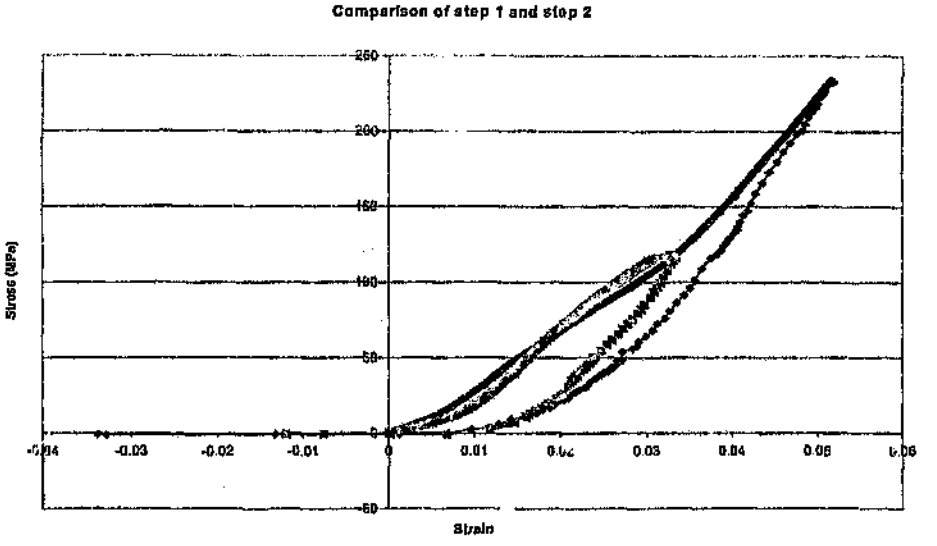


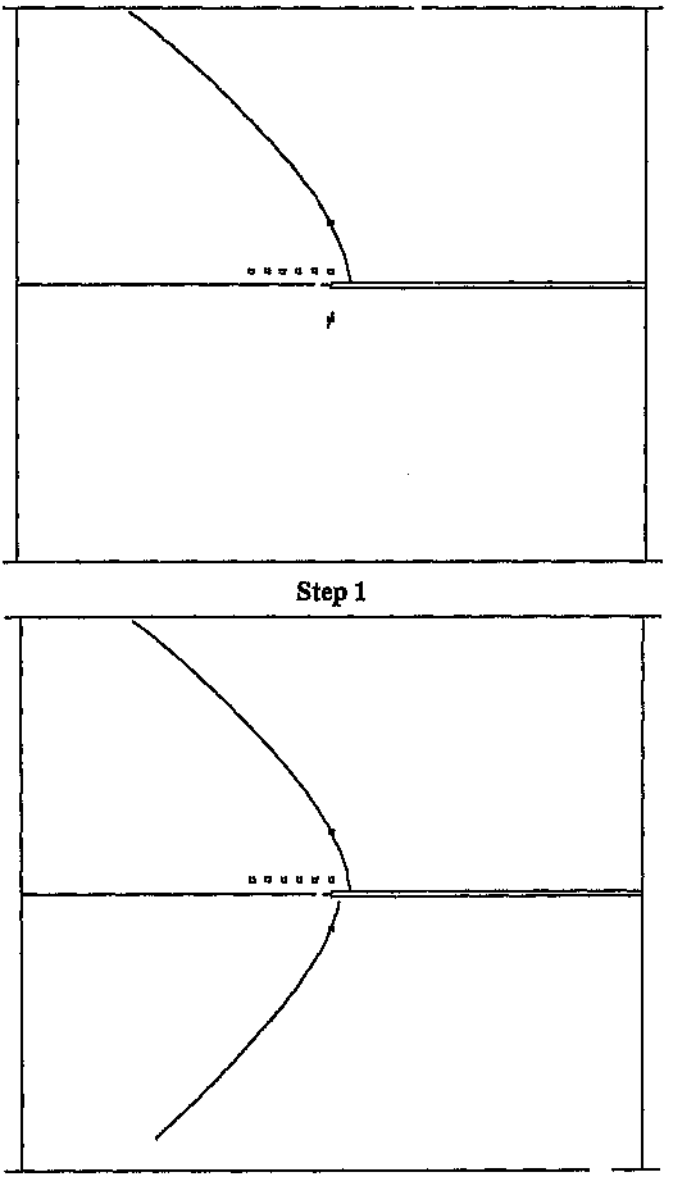
Figure 5.1.1 : Stress strain data for the case for no closure. The pink line representing the first step and the blue line the 2nd step.

In the first step, very little fracturing occurred. Proof of this could be seen in the steepness of the curve representing the first step. In the second step of mining, there is a shallower slope between the stresses of 90 MPa and 120 MPa after which the slope becomes steep again. This is most likely the period at which most fracturing took place in the sample. When using DIGS to simulate the fracture patterns, the sample cannot be loaded by fractions of a millimetre at a time due to computer storage limitations. The sample is therefore loaded in three increments. These increments are calculated by dividing the total amount of strain recorded in the physical sample and divided by three. For this reason, the exact stress at which fracturing takes place cannot be pinpointed. A range of stresses in which fracturing took place can be calculated. For this simulation the stress range at which fracturing took place was between 75 and 115 MPa. A similar range to that obtained during the physical experiment.

VI Fracture formation when mining in a solid block

In this series, the specimens were also prepared from Elsburg Quartzite. Mining steps were simulated by extending the length of the stope by approximately one millimetre after each test. A total of seven mining steps were tested and the resulting fracture patterns and the extent of the closed area in the stope were recorded for each of steps. For the numerical modelling, the fracture seed points are positioned close to the stope where the higher stresses exist and thus fracturing is expected to occur. The shear growth rule is specified on each crack with an initial cohesion of 35 MPa, initial friction angle of 35°, dilation angle of 5° , no residual cohesion, a residual friction angle of 32°, and a tensile cut-off of 5 MPa. A termination rule is specified so that the growth of a fracture would be terminated on intersection with another fracture. Figures 6.1 and 6.2. summarize the results from this series of testing. In both the physical and the numerical models, the fractures, which form in the first step, extend ahead of the face, both in the footwall and the hangingwall, until almost intersecting with the outer boundary. Subsequent steps in both the experiment and the simulation resulted in shorter fractures, in much the same direction as the initial fracture. Figure 6.2. shows the fracture patterns observed from modeling and testing after the last mining step. The orientation and length of fractures show overall similarities in both cases, although more damage at grain size level is prevalent in the physical model. Also, in the physical model, the major fractures were observed to consist of sets of small en-echelon fractures. These en-echelon fractures would indicate that the mode of failure was shear fracture (Kranz, 1983; Lockner et al. 1992). This indicates that the shear criterion used in the numerical solution is most likely to be valid for modeling shear fractures in the Quartzite rock. As there is a close correlation in terms

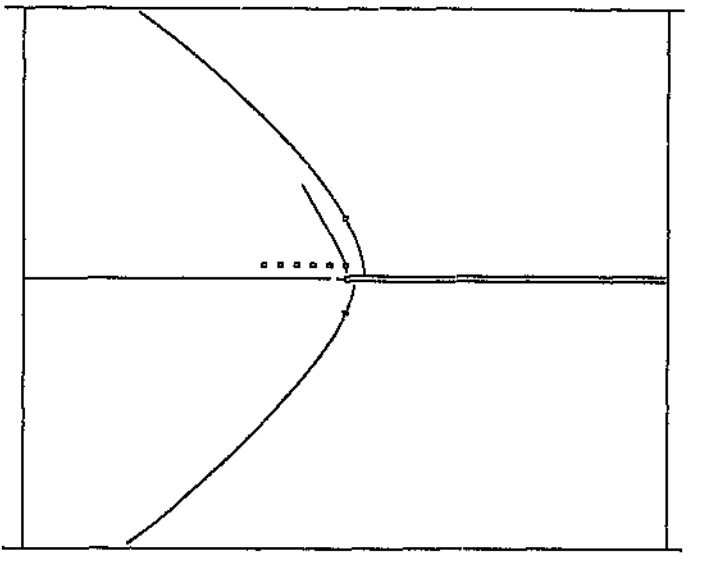
of length and direction of the shear fractures between the physical and the numerical case.



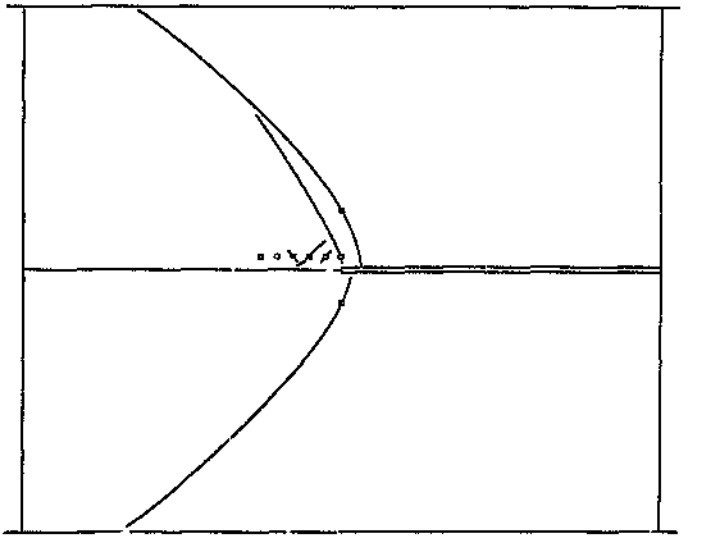
Step 1

Step 2

Figure 6.1. Fracture patterns obtained from DIGS for the "solid block" case. Step 1 and 2.

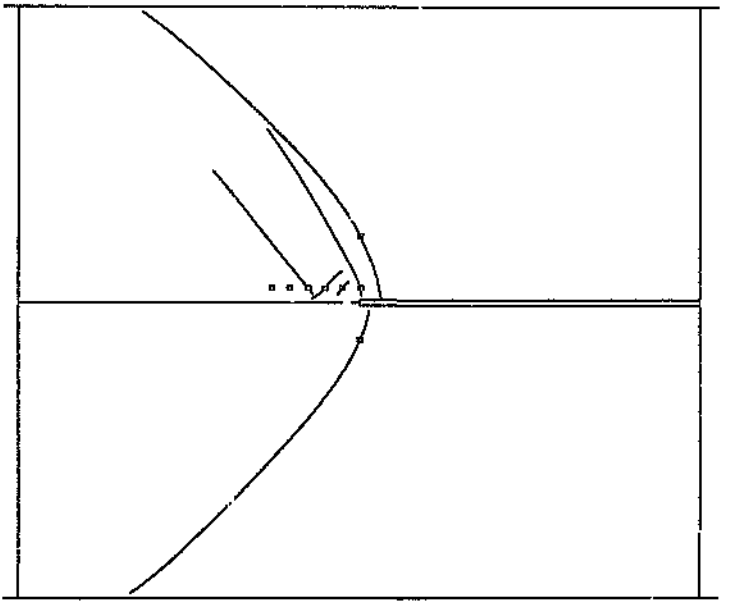


Step 3

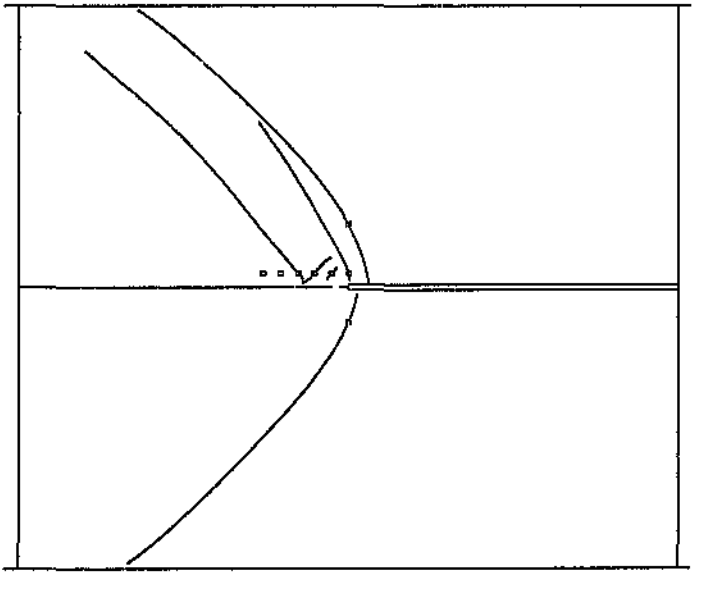


Step 4

Figure 6.1. Fracture patterns obtained from DIGS for the "solid block" case. Steps 3 and 4.

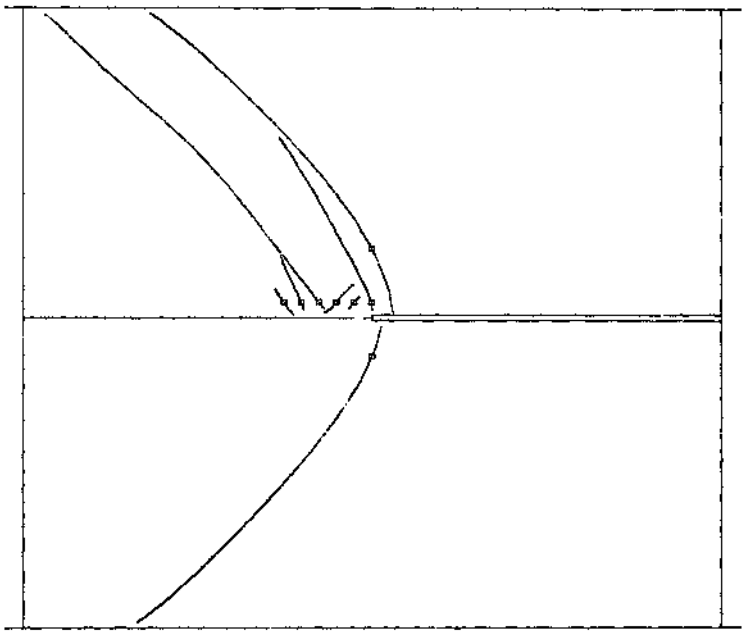


Step 5



Step 6

Figure 6.1. Fracture patterns obtained from DIGS for the "solid block" case. Step 5 and 6.



a:



b:

Figure 6.2. Comparison of "solid block" experiments at the seventh mining step, (a) being the numerical simulation and (b) the physical experiment.

6.1.1 Displacement versus load curves

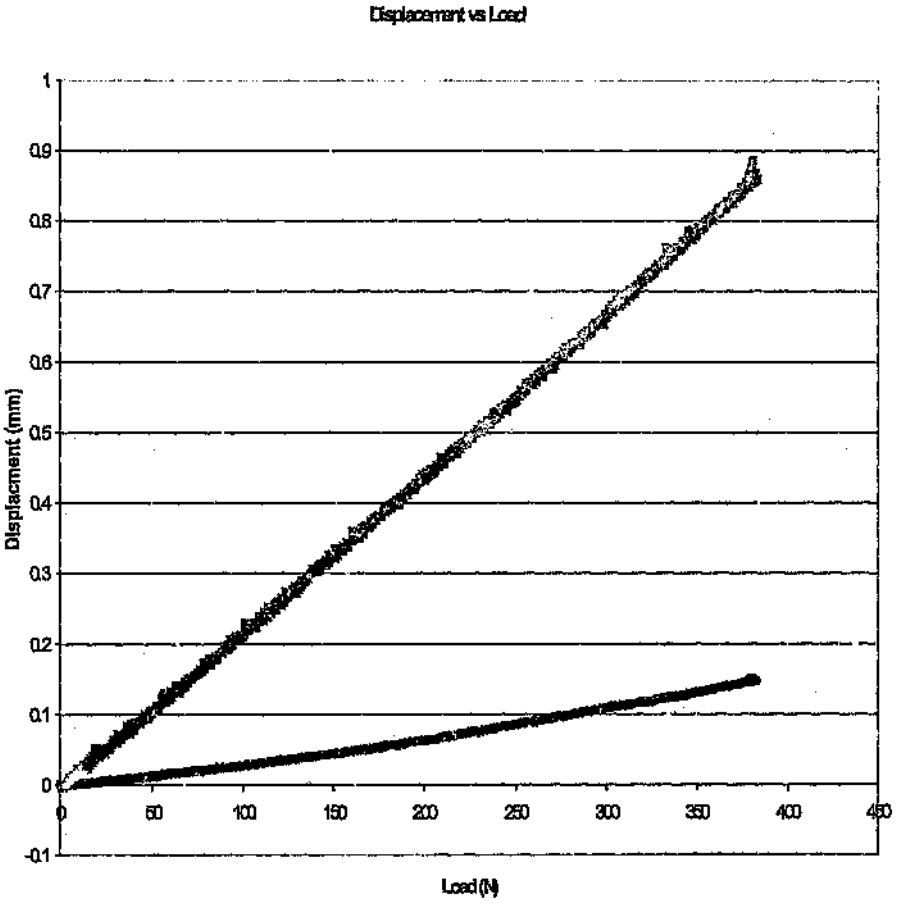
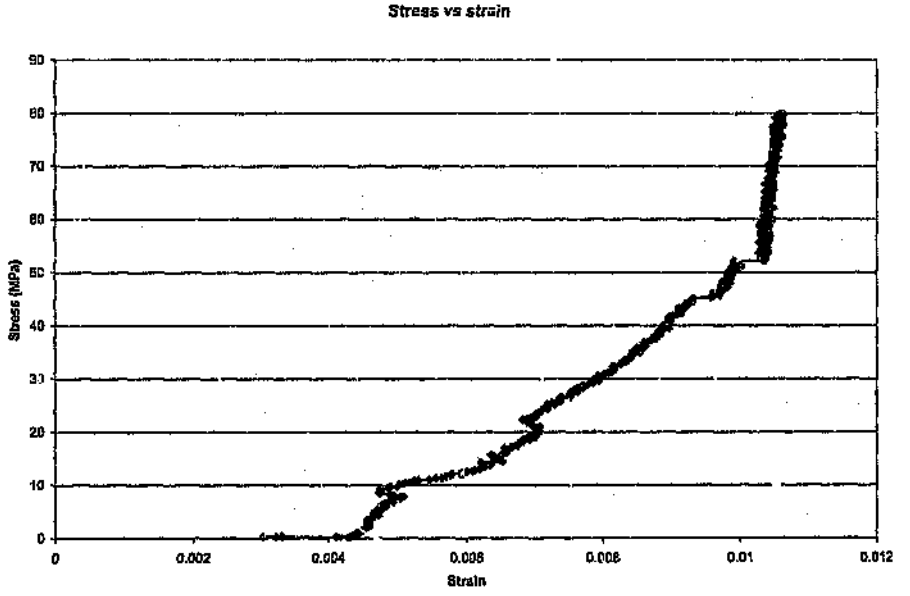


Figure 6.1.1.1 Displacement versus Load curve, the purple line indicating vertical displacement and the blue line indicating horizontal displacement.

The load versus displacement curve in figure 6.1.1.1. shows a higher vertical displacement as opposed to the horizontal displacement under the same vertical loading conditions. This difference in displacement defines the poisson's ratio for the test carried out. This particular test resulted in a poisson's ratio of 0.17. Poisson ratio

indicates that for one millimetre of displacement in the vertical direction, only 0.17 millimetres of displacement will occur in the horizontal direction. Very little irregularities occur on the graph. This would indicate that fracturing occurred regularly during the experiment rather than at a specific load.

6.1.2. Stress versus Strain



6.1.2.1. Stress vs Strain curve, with mining in a solid block, the 3rd mining step.

Determining the point at which fracturing took place during this step. The initial loading of the sample resulted in irregular strain patterns. This is due to the differing rates of vertical and horizontal loading. If the two rates were not increased at the same rate the resulting effect was the irregular stress strain pattern. From 22 MPa, this rate became the same. The stress at which fracturing most likely took place would be the points at which little stress is applied for a large amount of strain. This would be indicated on the graph by short horizontal lines. It is reasonable to assume therefore that fracturing took place where there are short horizontal lines. This occurs at a stress

of 47 MPa and 52 MPa. After which the curve becomes very steep, indicating an increase in strength of the sample. This same procedure was simulated on DIGS. Again only a range in which fracturing took place can be identified. This range was between 75 MPa and 115 MPa. This would indicate that the rock parameters input into DIGS are not accurately predicting the failure of the rock. This is indicate by comparing the ranges between which fracturing occurred. The physical model fractured between 47 and 52 MPa while for the numerical case the range of fracturing was between 75 and 115 MPa. The input parameters, based on Dede's (1996) work for the strength of the rock in DIGS are too high. These input parameters are, initial cohesion 35 MPa, initial friction angle 35 MPa, dilation angle 5 degrees, residual friction angle 32 degrees, tensile cutoff 5 MPa and the termination rule is specified.

Although these stress strain and displacement versus load curves do not give an indication of the direction of the fracturing, with the use of these curves, it is possible to obtain positions at which fracturing took place, as well as characteristics of the rock sample being used.

This is important as it enables more accurate parameters to be input into DIGS, for example the Poisson's ratio, while also allowing comparisons to be made, in-terms of the stress at which fracturing occurred.

Although these stress strain curves do not give an indication of the direction of the fracturing, with the use of these diagrams, it is possible to obtain positions at which fracturing took place, as well as characteristics of the rock sample being used.

This is important as it enables more accurate parameters to be input into DIGS, eg Poisson's ratio, while also allowing comparisons to be made in terms of the stress at which fracturing occurred.

Figure 6.1.1.1. indicates the horizontal displacement versus the vertical displacement. By dividing the horizontal displacement by the vertical displacement, we get the Poisson's Ratio. This ratio can be an accurate input into DIGS, which will allow for a better comparison between the physical and the numerical experiments.

Figure 6.1.2.1. indicates the positions at which fracturing took place, indicated by the short horizontal lines. The last part of the experiment, from 52 MPa and upwards, indicates a strengthening of the sample. This is shown by a sharp increase in the load, for very little strain. It is a reasonable assumption that the fractures have now closed up, and the sample is taking load.

The parameters input into DIGS were determined by Dede (1996). Although the samples used by Dede (1996) were quartzite, as is the case in this dissertation, the parameters used in this dissertation may therefore be slightly inaccurate. The samples, although both made from quartzite, may have come from different areas which would cause them to have different characteristics.

These parameters were defined by Dede (1996) with a 90 % confidence level. This could lead to further inaccuracies as a 10 % movement in either direction will vastly alter the parameters which are currently being input into DIGS.

6.2 Orientation of Fracturing

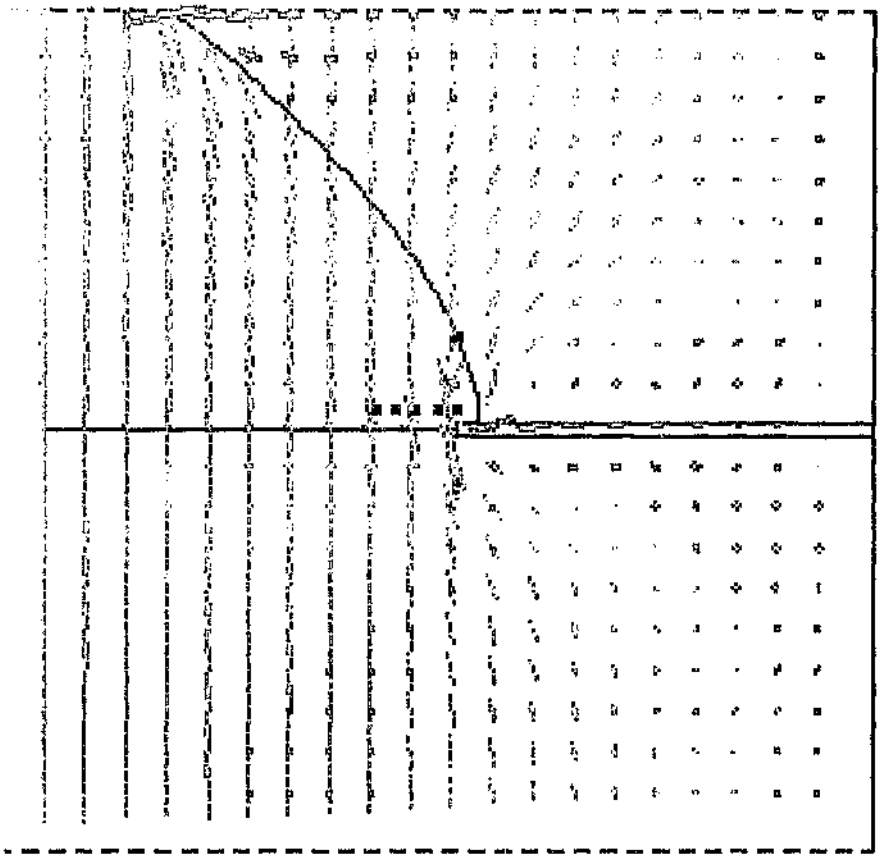


Figure 6.2.1. DIGS output showing Principle Stress direction.

Figure 6.2.1 shows the output from DIGS showing the principle stress directions. The direction of fracturing is directly related to the direction of the major principle

stresses. Close to the stope the fracture are almost vertical and so are is the direction of the fracture. However, as the fracture moves away from the stope, to the fracture levels out. This is caused due to the angle of the major principle stress also leveling out. This backs up the theory of Rorke and Brummer (1984) who said that the fractures formed in the direction of the major principle stress. It is known that in the underground situation there is a tensile zone that stretches for some metres into the hangingwall directly above the stope. From figure 6.2.1. a similar scenario can be seen with the stresses being in tension directly above the stope (the red markings indicate the presence of tensile stress, the longer the marker the higher the tensile stresses).The direction of the shear stresses are also similar to the stress directions found underground. The stresses underground near a stope are re-distributed by bending around the stope in a bow shape, similar to what can be seen in figure 6.2.1.

6.3 Results from DIGS tesselation simulations

A parametric study was carried out using DIGS; the tesselation approach. The effects of changing various parameters including mobilised cohesion, Young's modulus, Poisson's ratio and un-mobilised cohesion were studied.

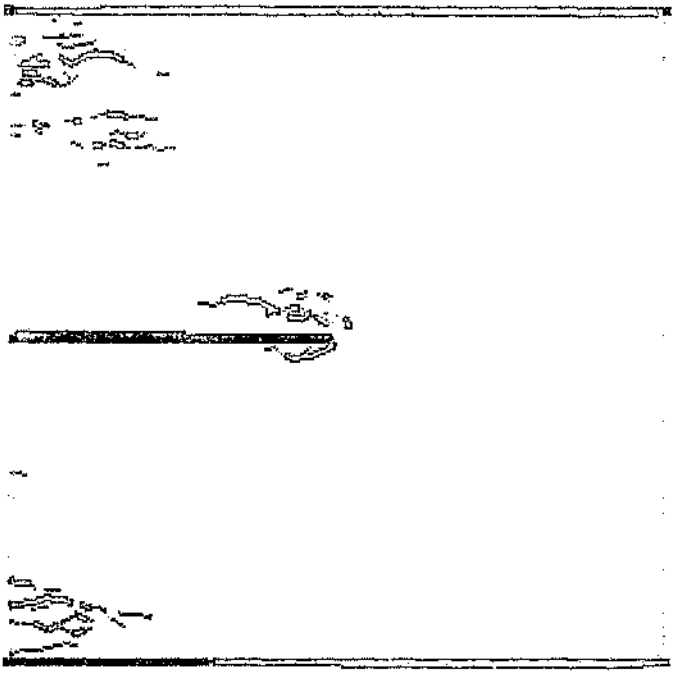
6.3.1 Poisson's Ratio

Changing the Poisson's ratio resulted in the following outputs. Figure 6.3.1.1.(a) had a Poisson's ratio of 0.15 while figure 6.3.1.1(b) had a Poisson's ratio of 0.20. For both outputs, the mode and direction of failure correlates well with the physical tests as no stope closure existed in these tests. In Figure 6.3.1.1.(a), extended lateral fracturing

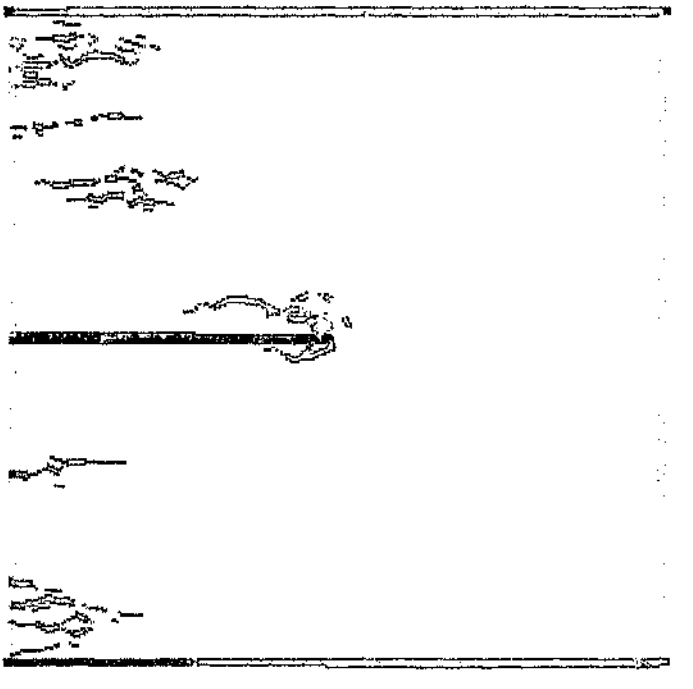
occurred near the face as opposed to figure 6.3.1.1.(b). This can be attributed to the lower Poisson's ratio. Limiting the Poisson's ratio to 0.15 and not 0.20, doesn't allow as much horizontal fracturing to occur, but the vertical stress is not lowered, therefore the same amount of energy exists in the sample. Releasing this energy takes the form of more fracturing. An important part of the fracture growth and initiation is shown in the DIGS outputs. The horizontal fracturing above and below the stope is parallel to the boundary. This same phenomenon was observed in the physical sample.

6.3.2 Young's Modulus

The Young's Modulus was varied from 70 GPa to 55 GPa. The outputs are shown in Figure 6.3.2.1 (a) and (b). Figure 6.3.2.1.(a) has a Young's Modulus of 55 GPa while Figure 6.3.2.1.(b) has a modulus of 70 GPa. As can be seen in the figure, a higher Young's Modulus results in less fracturing. With a higher Modulus in Figure 6.3.2.1(b) and the same stress state in both cases, less fracturing should occur as less areas in the sample reach the fracture barrier. In both figures the orientation and mode of failure is as expected with no stope closure occurring.

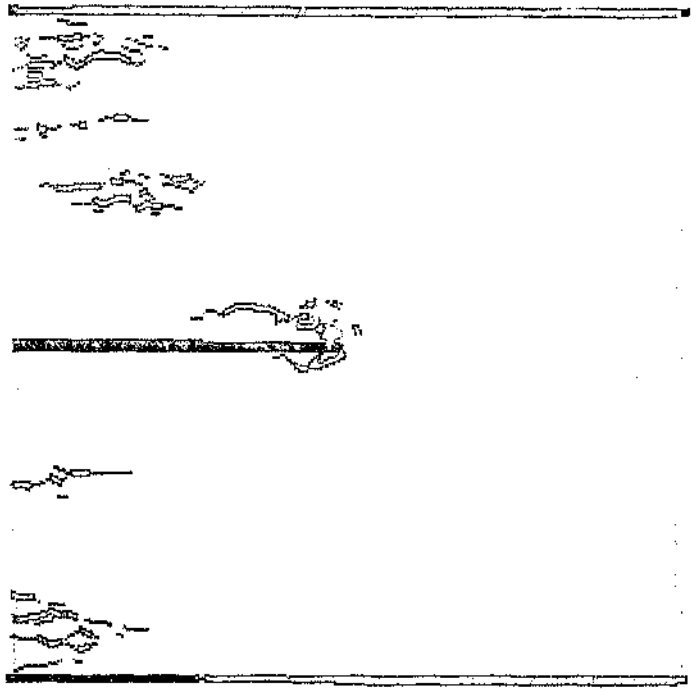


(a)

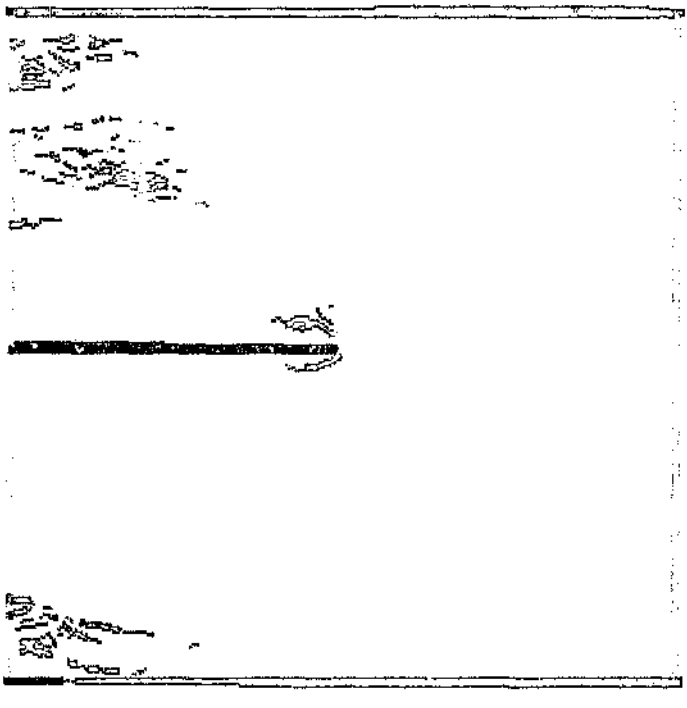


(b)

Figure 6.3.1.1. Outputs from DIGS tesselation showing the effects of varying the Poisson's Ratio. (a) with a poisson's ratio of 0.15 and (b) of 0.20



(a)



(b)

Figure 6.3.2.1. Outputs from DIGS tesselation showing the effects of varying the Young's Modulus. (a) has a Young's Modulus of 55 GPa and (b) has a modulus of 70 GPa.

6.3.3 Mobilised Cohesion

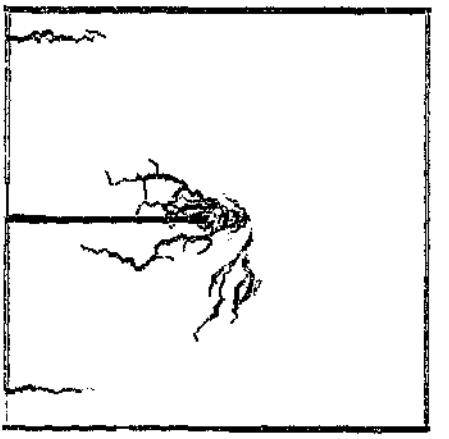
Mobilised cohesion was varied between 5 MPa and 30 MPa. Figures 6.3.3.1. (a), (b), (c) show the different resulting fracture patterns of having mobilsed cohesion of 5, 15 and 30 MPa respectively.

All other parameters remained constant. For all three cases, the direction and mode of failure is correct according to the physical experiments. Figure 6.3.3.1 (b), compares most favourably with the fracture pattern of the physical experiment. The mode of failure in these cases was tensile failure with no stope closure occurring. Less fracturing was observed when comparing Figure 6.3.3.1 (a) with Figure 6.3.3.1 (b). Figure 6.3.3.1 (b) having the higher mobilised cohesion. In Figures 6.3.3.1 (a) and 6.3.3.1 (b) most of the fracturing occurred in the footwall. In Figure 6.3.3.1(c), which has the highest mobilised cohesion, most of the fracturing occurred in the hangingwall. The amount of fracturing is comparable to Figure 6.3.3.1. (a).

A variation of the mobilised cohesion would allow for fractures to grow more easily, the lower the mobilised cohesion value. For instance the fractures for the lower mobilised cohesion value should be longer than the fractures with a higher mobilised cohesion value. This is because once the fracture has been started, the lower mobilised cohesion value allows this fracture to grow more easily.

6.3.4 Unmobilised Cohesion

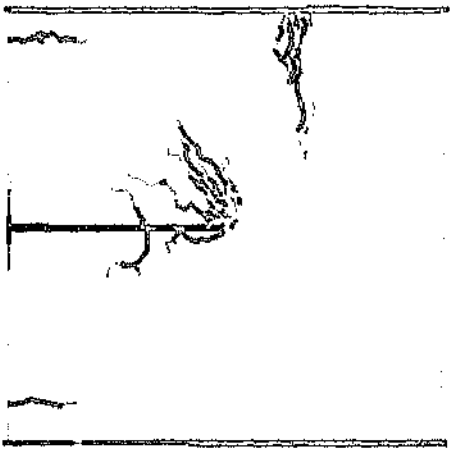
Figures 6.3.4.1. (a) and (b) show the results of varying the unmobilised cohesion. Figure 6.3.4.1. has an unmobilised cohesion of 20 MPa while figure 6.3.4.1 (b) has 35 MPa unmobilised cohesion. Both results have the correct direction and mode of failure according to the physical experiments.



(a)

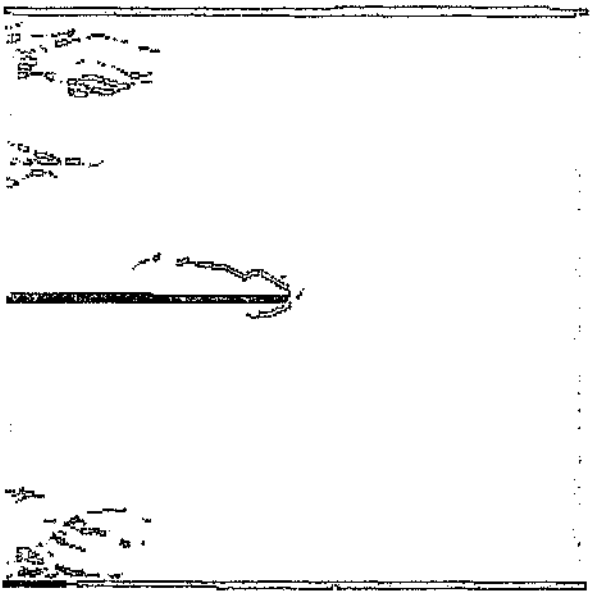


(b)

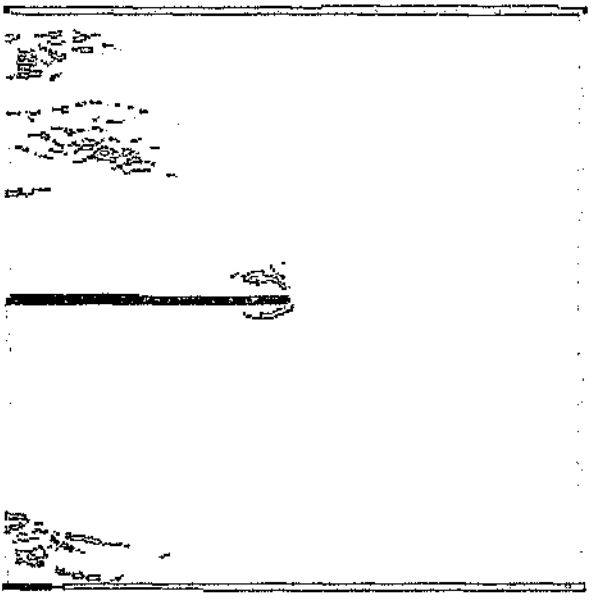


(c)

Figure 6.3.3.1. Outputs from DIGS tesselation showing the effects of Mobilised Cohesion. (a) has a mobilised cohesion of 5 MPa, (b) of 15 MPa and (c) of 30 MPa



(a)



(b)

Figure 6.3.4.1. Outputs from DIGS tesselation showing the effects of Unmobilised Cohesion. (a) has an unmobilised cohesion of 20 MPa and (b) of 35 MPa.

The fracturing resulting because of the stope is longer in Figure 6.3.4.1(a) compared with Figure 6.3.4.1(b). This is as a result of the lower unmobilised cohesion value. It is easier for the fracturing to continue as there is less stress in the non-fractured material. More fracturing occurs in the hangingwall boundary above the stope in Figure 6.3.4.1 (b) which has a higher unmobilised cohesion.

6.3.5 Conclusions about DIGS tesselation

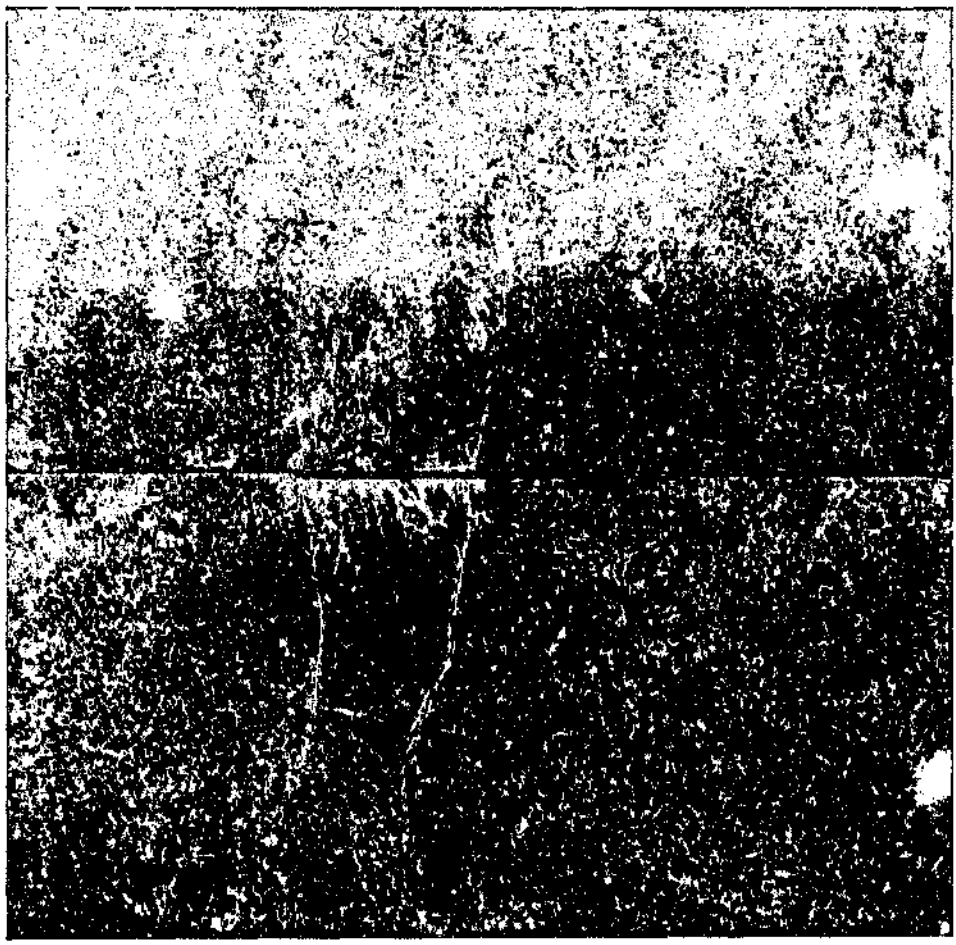
With the DIGS tesselation version, it eliminates the need
to select seed points, as a pre-defined grid of possible fractures is superimposed onto the given geometry. It is necessary to select the correct parameters which determines the mode of failure. The results shown previously indicates the DIGS tesselation versions ability to predict the position of fracture initiation and the mode of failure, given the correct failure parameters.

The parameters which gave the closest correlation with the physical experiments were an initial cohesion of 35 MPa , initial friction angle of 35°, dilation angle of 5°, no residual cohesion, a residual friction angle of 32°, and a tensile cut-off of 5 MPa. A termination rule is specified so that the growth of a fracture would terminate on intersection with another fracture.

VII Effect of a discontinuity on the final Fracture Formation

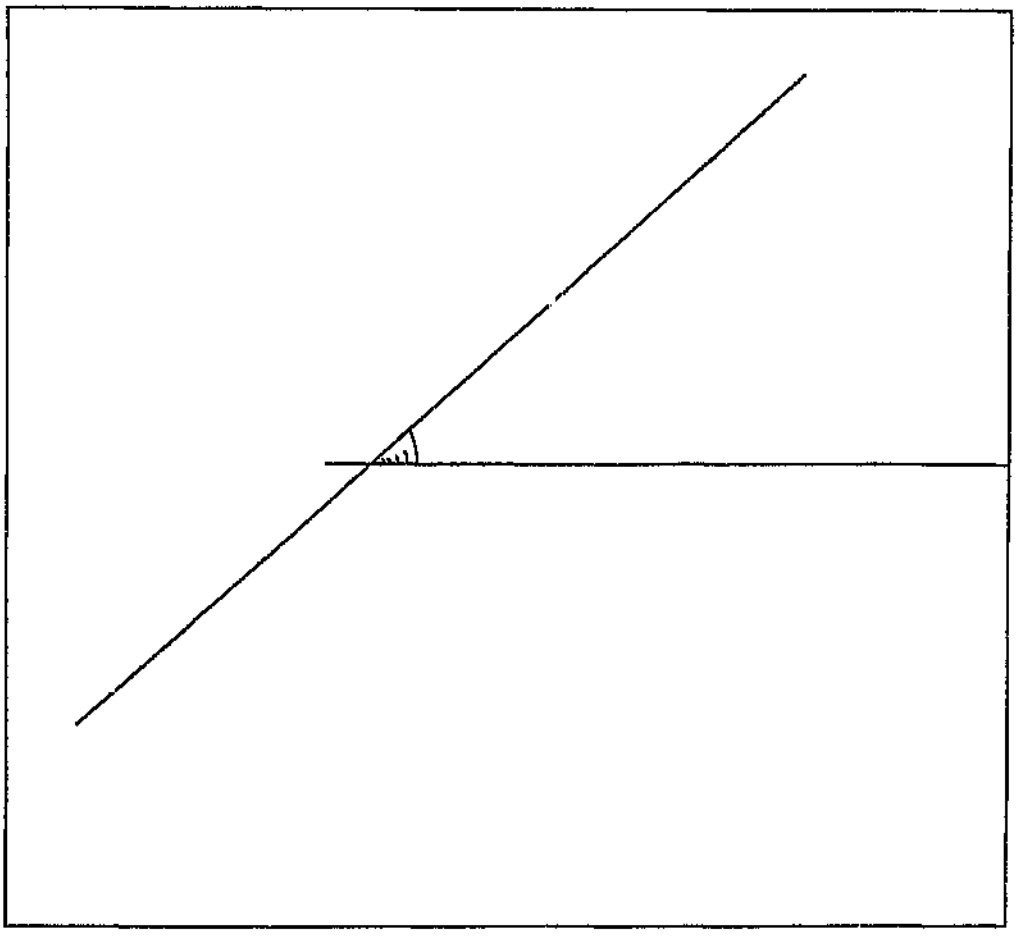
7.1. Physical Models

Two samples of Elsburg Quartzite were tested to investigate the influence of a pre-existing discontinuity on the fracture pattern around the slot. This situation can be thought of as a small scale representation of mining towards a fault. The one sample was free of visible discontinuities and was machined according to the standard procedure shown in Figure 6.2. Another sample was machined with an existing discontinuity plane at an angle to the slot. The plane consisted of a welded joint with quartz infilling and was angled so that it passed through the centre point of one side of the sample. The test involved sequential machining of the slot towards the discontinuity. Figure 7.3.1. shows the effect of the discontinuity of the final fracture pattern.



a:

Figure 7.1.1: Schematic of fracture patterns observed in physical models. a: side with discontinuity close to slot



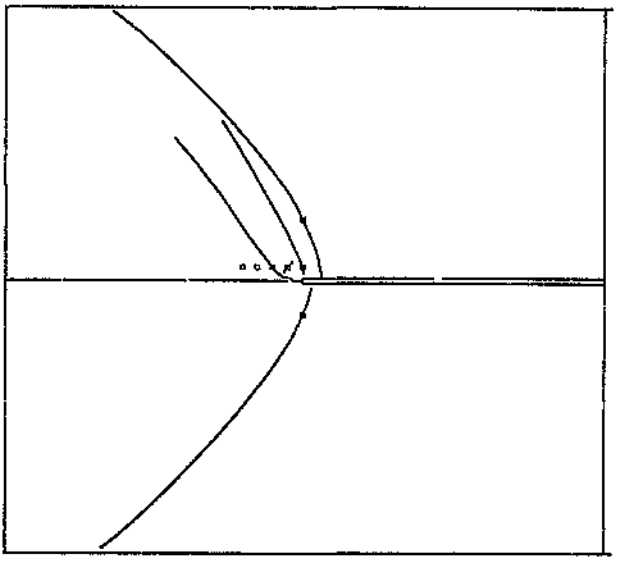
b:

Figure 7.1.1: Schematic of fracture patterns observed in physical models. a: block without discontinuity, b: side with discontinuity close to slot, c: opposite side with discontinuity further from slot

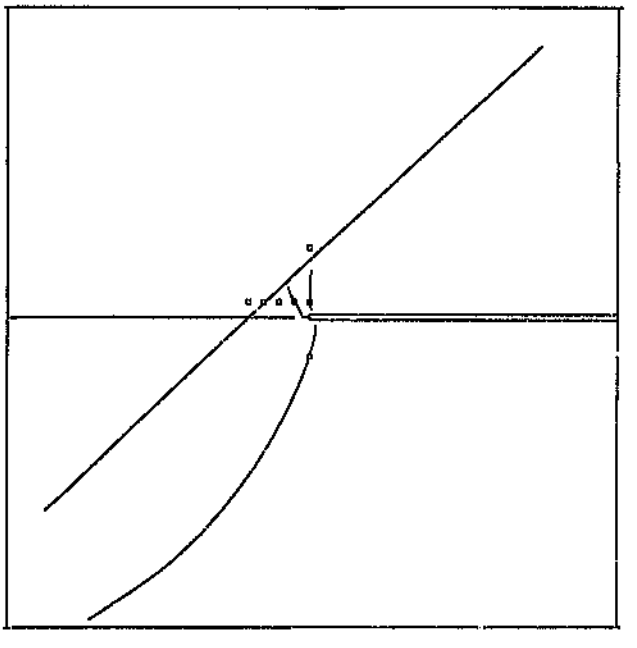
7.2. Numerical Simulations

In numerical simulations, a constant confining pressure of 27 MPa is applied to the sides of the sample. The sides and base contacts are modelled to be frictionless. The vertical loading is generated from uniform vertical displacement. The sample without discontinuities can be represented by a single plane strain approximation. Two analyses were required to investigate the effect of discontinuites because of the different distances between the slot and the angled discontinuity on either side of the sample.

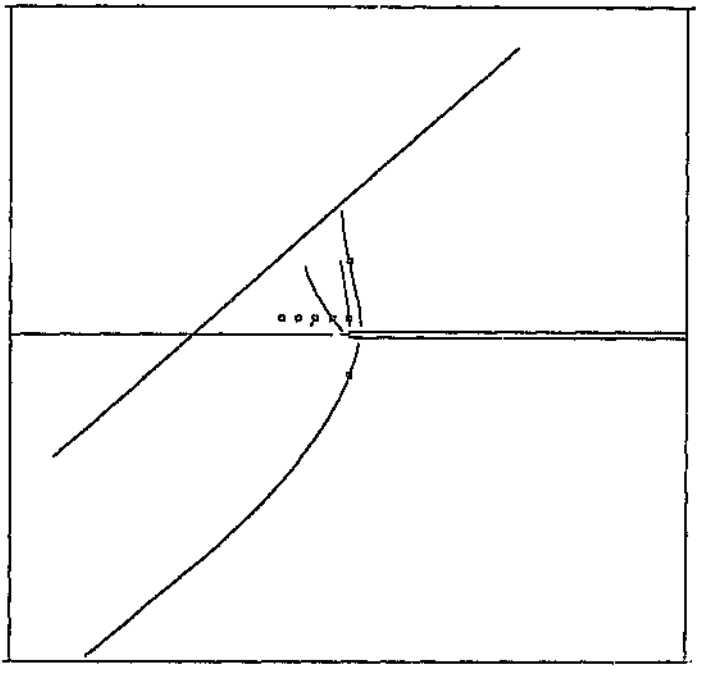
The slot was modelled by having no normal or shear stress and a limited amount of closure, corresponding to the slot width of 0.5mm. Material properties for this simulation were a Poisson's ratio of 0.17 and a Young's Modulus of 68 GPa. The fracture seed points are positioned close to the slot as this is where the high stresses are expected to occur and hence failure is likely to take place. The shear growth rule is specified on each crack with an initial cohesion of 35.1 MPa, initial friction angle φ of 35°, dilation angle of 5° , no residual cohesion, a residual friction angle of 32°, and a tensile cut-off of 5 MPa. A termination rule is specified so that the growth of a fracture would be terminated on intersection with another fracture. The discontinuity characteristics are defined as having an unmobilised cohesion of 5 MPa, an unmobilised friction angle of 20 degrees, a mobilised dilation angle of 5 degrees, a mobilsed friction angle of 15 degrees and has zero mobilised cohesion.



a:



b:



c:

Figure 7.2.1.: Fracture patterns predicted in numerical simulations. a: bl- c without discontinuity, b: discontinuity close to slot, c: discontinuity further from slot

The termination rule is also specified for the discontinuity, meaning that no fracture can continue to grow through the discontinuity. The results of the three analyses are shown in Figure 7.2.1.

7.3. Comparison of physical and numerical models

In the experiment (Figure 6.2) and the numerical model (Figure 7.2.1.b), the fractures which formed in the first step extend ahead of the face, both in the footwall and the hangingwall, until almost intersecting with the outer boundary. Subsequent steps in both the experiment and the simulation resulted in shorter fractures, in much the same direction as the initial fracture. In the experiment, the major fractures were observed to consist of sets of small, en-echelon, fractures. These en-echelon fractures would indicate that the mode of failure was shear fracture (Kranz, 1983; Lockner et al. 1992). This would provide confirmation that the shear criterion applied in the numerical solution, shown in Figure 7.2.1.a, can be applied for modelling shear fractures in the Quartzite rock.

The influence of the existing discontinuity can be seen by in Figures 7.1.1.a, 7.1.1.b, 7.2.1.b and 7.2.1.c. The physical and numerical models show similar fracture patterns. In all cases, a footwall fracture extends ahead of the face in the first step, as was observed in the case without a discontinuity. A difference in the fracture pattern is apparent in the hangingwall block. The initial fracture was formed in much the same way as the homogeneous sample and terminated at the discontinuity. The fracture terminating at the point of intersection between the fracture and the discontinuity suggests that either the quartz infilling of the joint was too tough to fracture, or that the deformation was accommodated by activation of the discontinuity. Observation of the tested samples showed evidence that the discontinuity has been activated.

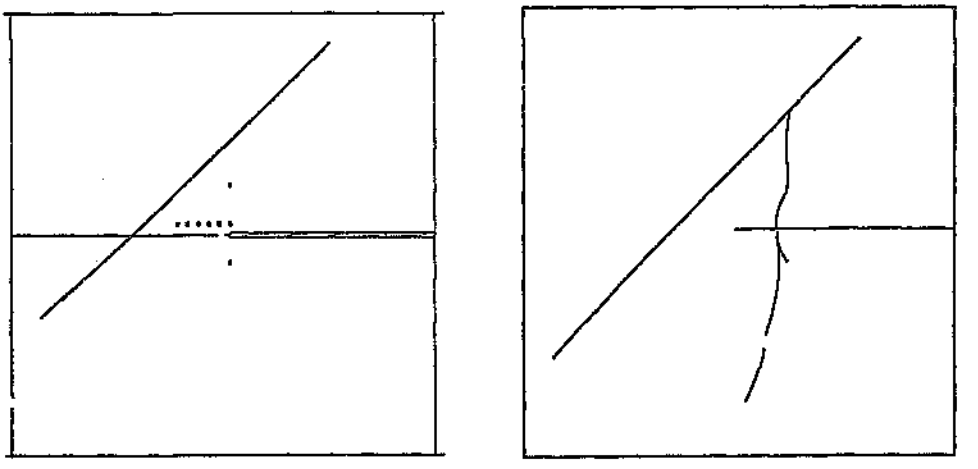
On the side of the block where the discontinuity intersects the slot, subsequent steps in the experiment showed little fracturing occurring in either the footwall or the hangingwall (Figure 7.1.1a). In the numerical solution, see Figure 7.2.1.b, a single fracture extended to the discontinuity, and then continued mining induced no more fracturing. On the other side of the block, smaller fractures extended in the same direction as the initial fracture, increasing in length with each mining step. Then, the eighth step of the experiment produced an extended fracture in the footwall, and no fracturing in the hangingwall. Finally, in the tenth step, one fracture extended from the corner of the slot to the discontinuity in the hangingwall, and another grew in the footwall towards the large fracture formed in the previous step. These results suggest that the deformation will occur preferentially on the largest existing weakness (e.g. fracture or discontinuity), until the stress state has been altered sufficiently to require the formation of a new fracture.

7.3. Comparison of step by step outputs for the physical and numerical simulations

In this experiment, 10 mining steps where carried out in the direction of the fault. The fracture pattern was recorded after each step. The same scenario was simulated using DIGS, unfortunately due to a DIGS limitation, only nine mining steps were simulated. Figure 7.3.1. gives a step by step comparison.

Numerical Modelling Physical Modelling

1st step



2nd step

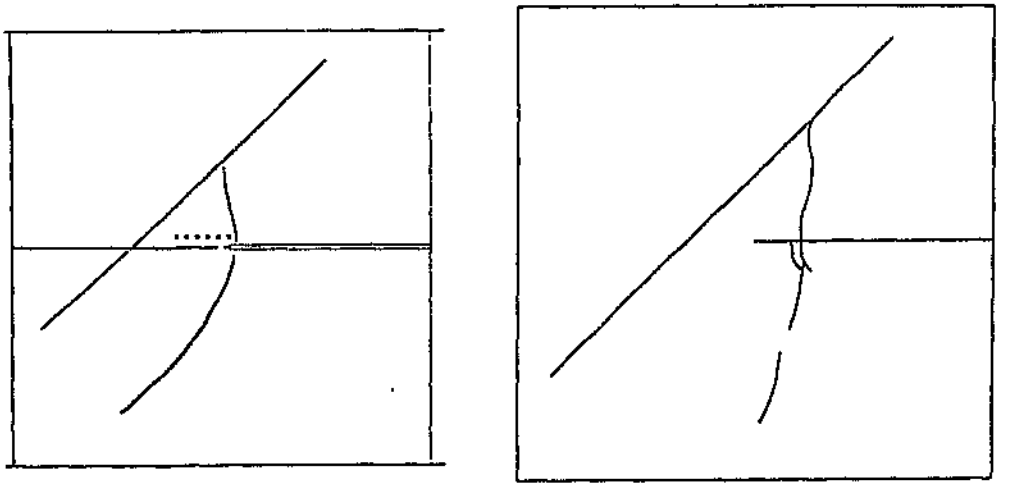
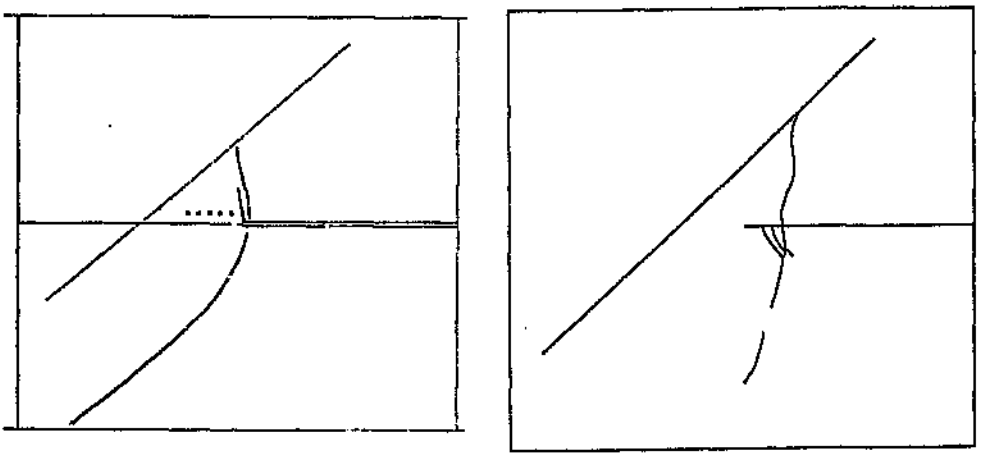


Figure 7.3.1. Step-by-step comparison of the Physical Experiments versus Numerical Simulations. Step 1 and 2.

Numerical Modelling Physical Modelling

3rd step



4th step

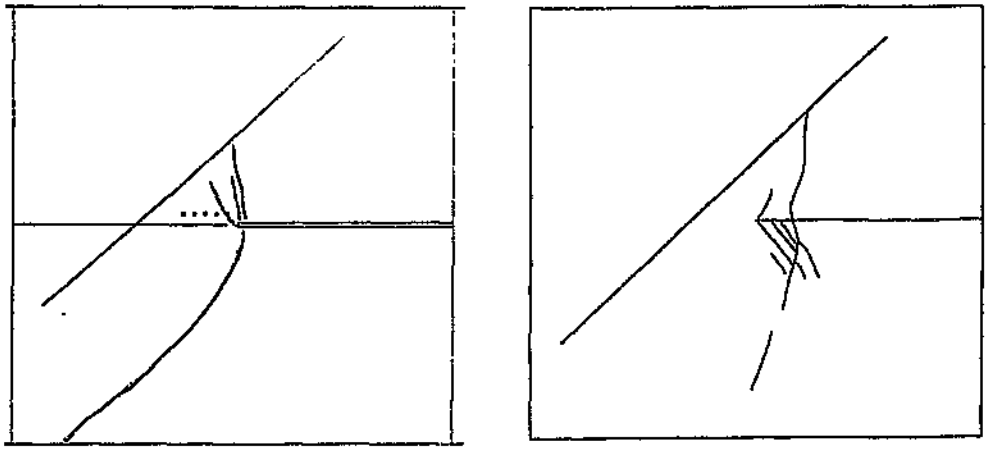
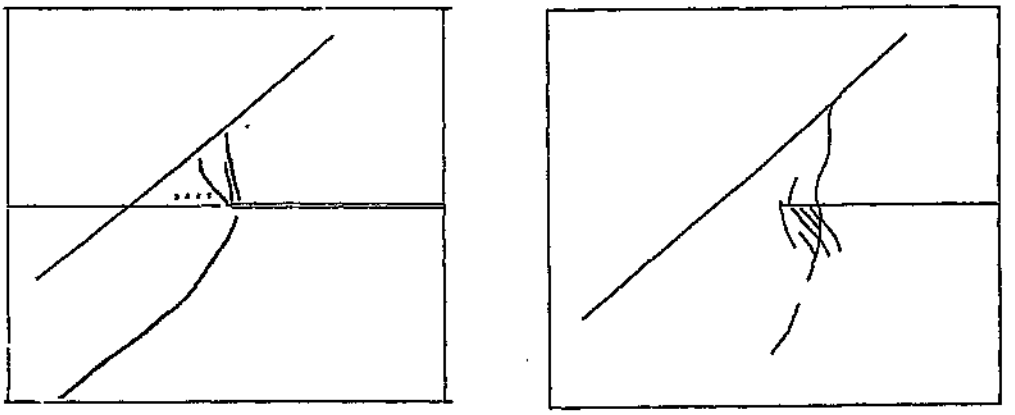


Figure 7.3.1. Step-by-step comparison of the Physical Experiments versus Numerical Simulations. Step 3 and 4.

Numerical Modelling Physical Modelling

5th step



6th step

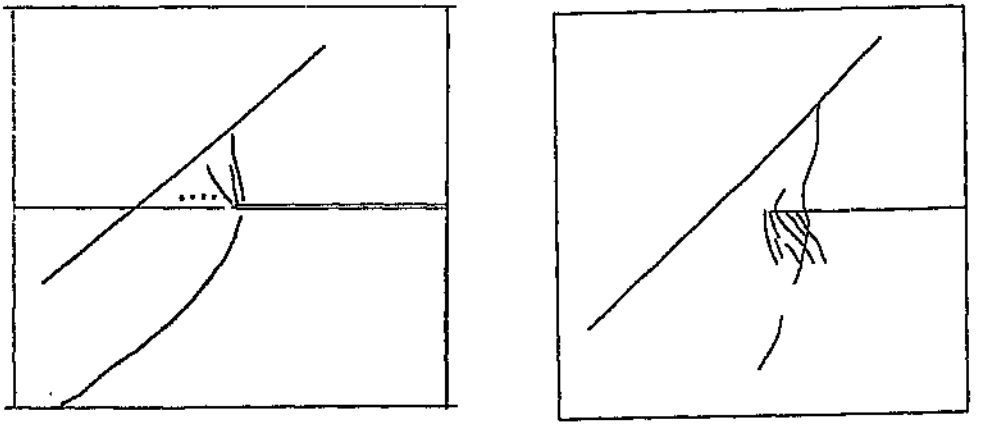
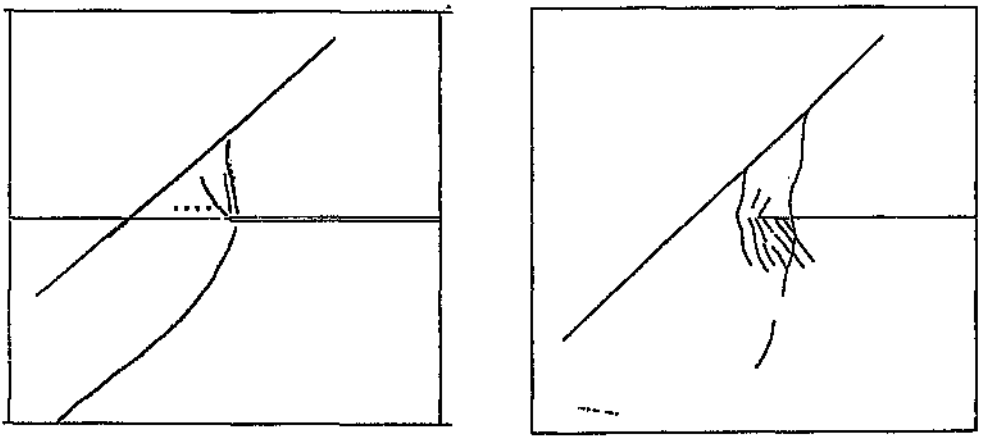


Figure 7.3.1. Step-by-step comparison of the Physical Experiments versus Numerical Simulations. Step 5 and 6.

Numerical Modelling Physical Modelling

7th step



8th step

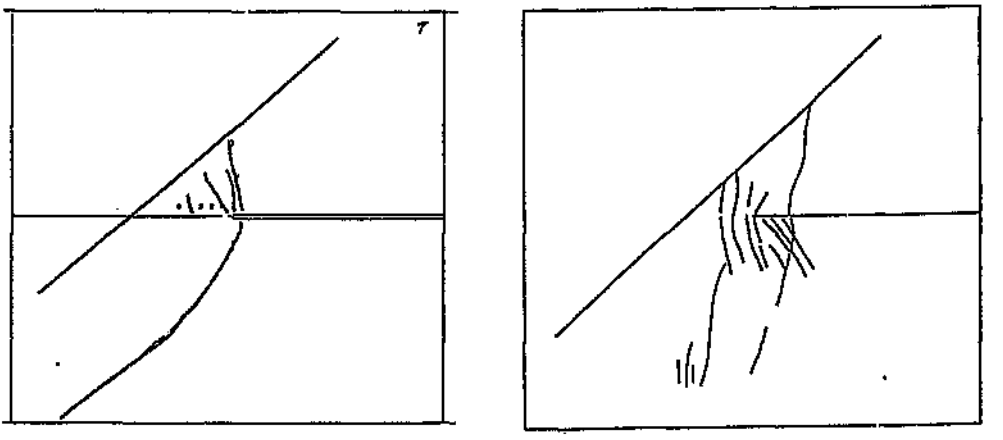


Figure 7.3.1. Step-by-step comparison of the Physical Experiments versus Numerical Simulations. Step 7 and 8.

Numerical Modelling **Physical Modelling**

9th step

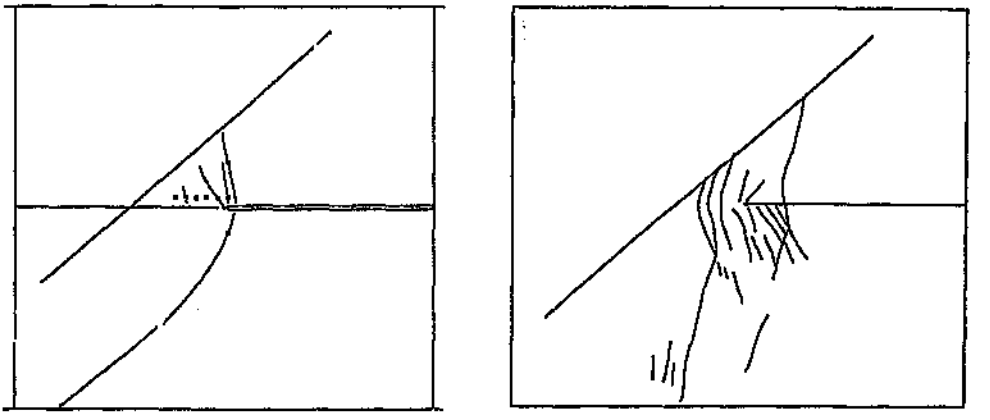


Figure 7.3.1. Step-by-step comparison of the Physical Experiments versus Numerical Simulations. the final step.

Studying these outputs from DIGS reveals its ability to correctly redistribute the stresses. The initial fracture intersecting the discontinuity ends its growth at the intersection because of the termination rule imposed on it. However, the fractures in subsequent steps do not extend up and intersect with the discontinuity. Compare the length of the fractures, with the discontinuity in figure 7.3.1. with the length of the fractures without the discontinuity in figure 7.2.1. It is evident that DIGS is redistributing the stresses in the case of the discontinuity resulting in the shorter fractures being formed after the first fracture which intersects with the discontinuity. These results are the same as were achieved in the physical experiments. Explanation of the shorter fractures in the subsequent steps was described earlier, but says that formation will preferentially occur on the largest existing weakness until the stress

state has been sufficiently altered to require the formation of new fractures. If this is a repeatable representation of what happens in the physical experiment and DIGS is correctly simulating the fracture pattern, then DIGS must be correctly simulating the stress state.

7.4. Simulated Orientation of Stresses

Figure 7.4.1. shows the result of DIGS when simulating the major principle stress directions. A tensile zone of stress exists directly above the discontinuity. Due to the stresses applied to the block and the parameters of the discontinuity moved of the rock into the mined out area could be taking place. The movement of the rock could be leading to the tensile zone which is apparent above the discontinuity.

At the lower extremity of the discontinuity another zone of tension exists indicated by the red markings. This could be the result of the movement of the rock due to the stresses imposed on the block. The fractures in the hangingwall tend to follow the direction of the major principle stresses. The fracture that extends into the footwall does not however follow this same convention. The orientation of this major principle stresses has no bearing on the direction of the fracturing taking place in the footwall.

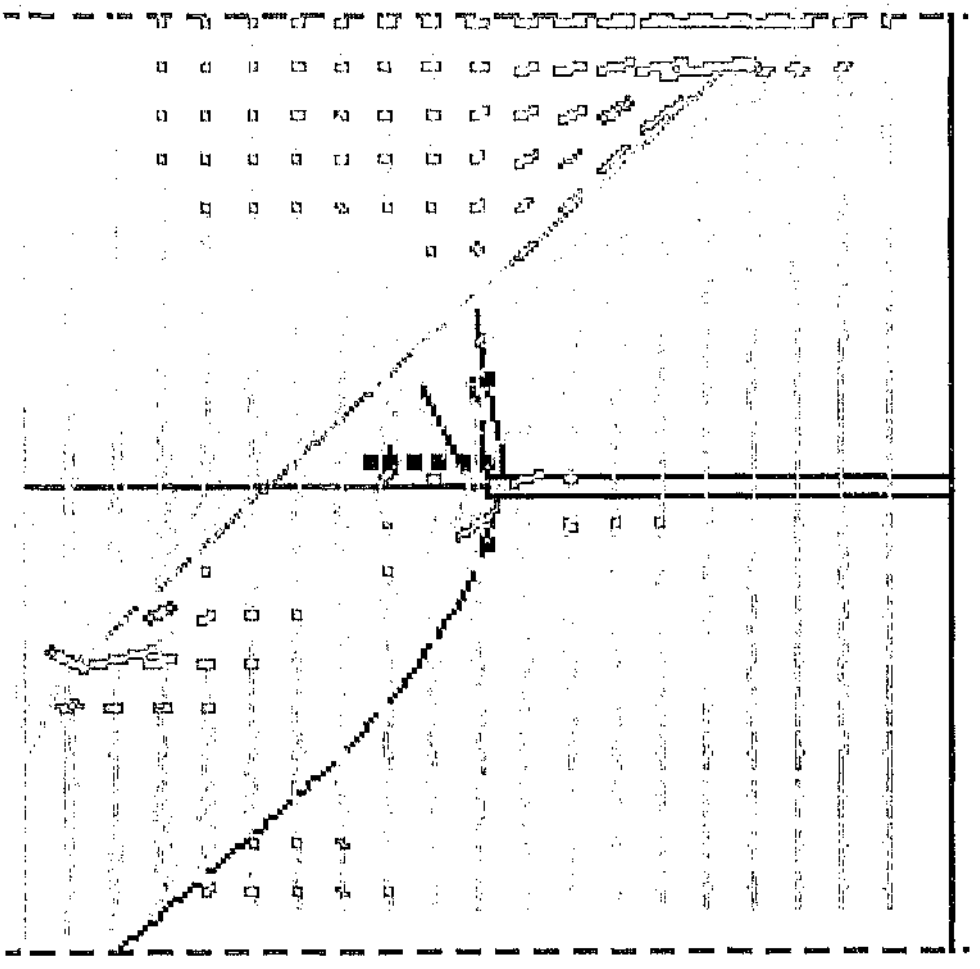


Figure 7.4.1. Output from DIGS Simulating the Stress Direction with an Existing Discontinuity

VIII Influences of Parting Planes on Fracture Formation around a Deep Level Stope

8.1. Physical Models

Two samples were prepared to compare the influence of parting planes on the final fracture pattern, each of Black Reef Quartzite. The first was an ordinary sample as shown in Figure 8.1.1 and the other sample consisted of 4 plates each 20mm thick. This sample represents an approximation of a rockmass containing a series of horizontal bedding planes. The friction angle on each interface was measured as 26 degrees. In both cases, the thickness of the slot was 0.5mm which was too large to induce closure of the slot in the stiffer Black Reef Quartzite.

8.1.1. Acoustic emission

Figure 8.1.1.1.a shows the located AE events in the sample without parting planes. Only events with amplitudes greater than 70dB are shown. The events are clustered in the same regions as the observed fractures. The events in the centre of the sample correspond to the fractures which curve into the hangingwall from the edge of the slot. The vertical fractures ahead of the slot, in the hangingwall and footwall are also evident. A cluster of events at the edge of the sample corresponds to the small horizontal fracture in the hangingwall.

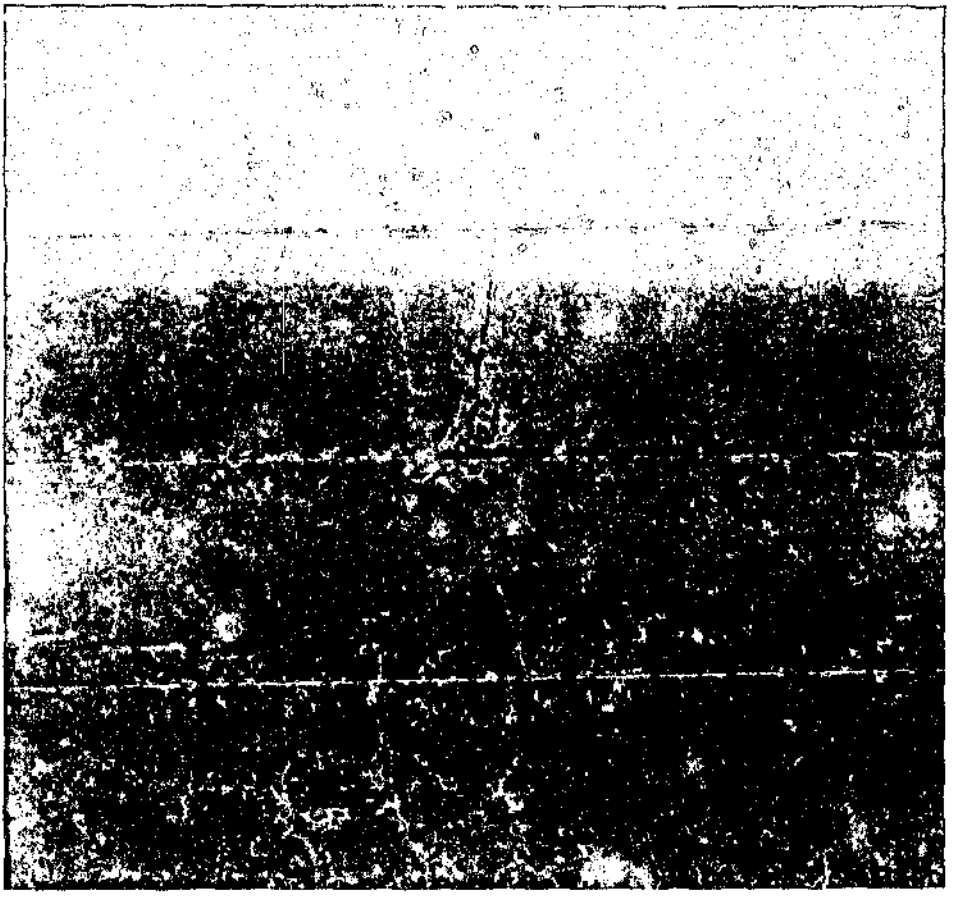


Figure 8.1.1: Schematic of fracture patterns observed in physical models using Black Reef Quartzite.

Two steps were undertaken with the sample containing parting planes and, in each step, the positions of the AE events (shown in Figure 8.1.1.1b) correspond closely to the cracks observed (Figure 8.1.1). In the first step, the vertical cracking is evident in the two footwall blocks, ahead of the stope. There is less AE activity in the immediate hangingwall block, and the located events correspond to the angled crack extending from the slot tip, and the small fractures which are initiated at the upper parting planes. In the top block, the events relate to the two vertical fractures ahead of the face. In the second step, the vertical fractures ahead of the slot extended through the sample and the angled cracks in the hangingwall connected the slot and the parting plane above, as shown by the AE events above the slot.

8.2. Numerical Simulations

For all the numerical simulations, plane strain conditions were considered. Two simulations were carried out, one with parting planes and one without. The material properties used in the simulations were a Young's Modulus of 78 GPa and a Poisson's ratio of 0.2. The parting planes had a friction angle of 26°. A tension mode of failure was selected for the cracks with zero tensile strength and a residual friction of 20°.

a:

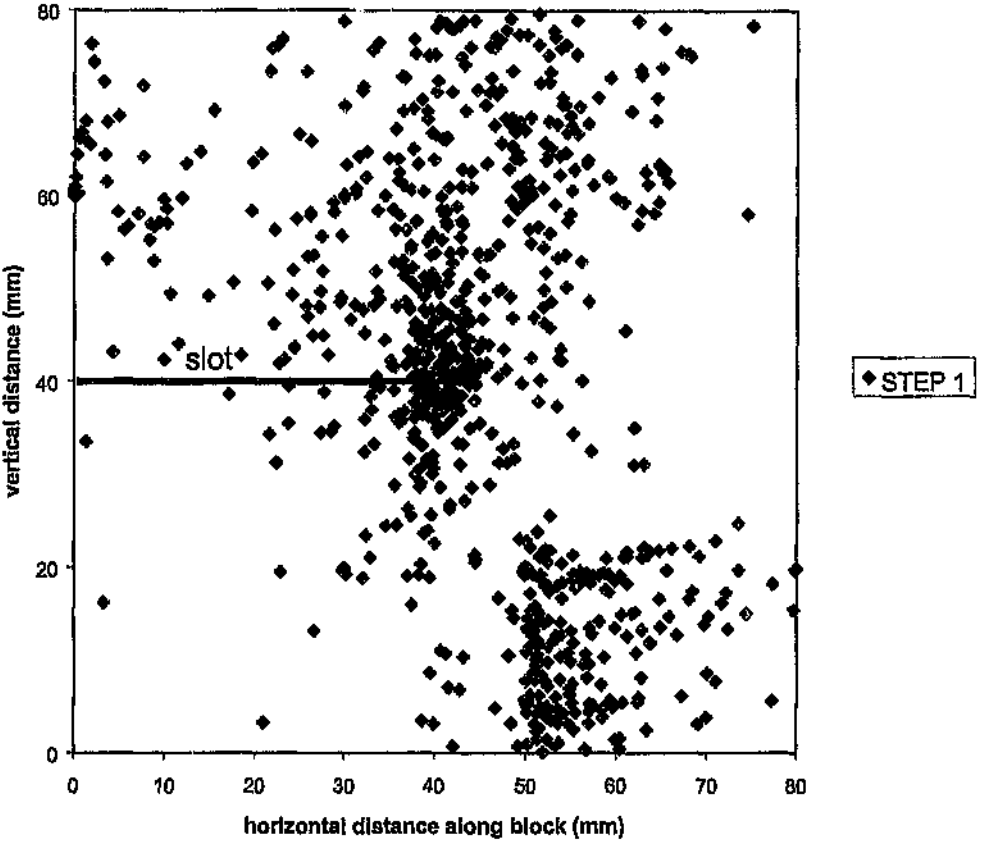


Figure 8.1.1.1: Locations of acoustic emissions determined in physical models using Black Reef Quartzite. a: block without discontinuity

b:

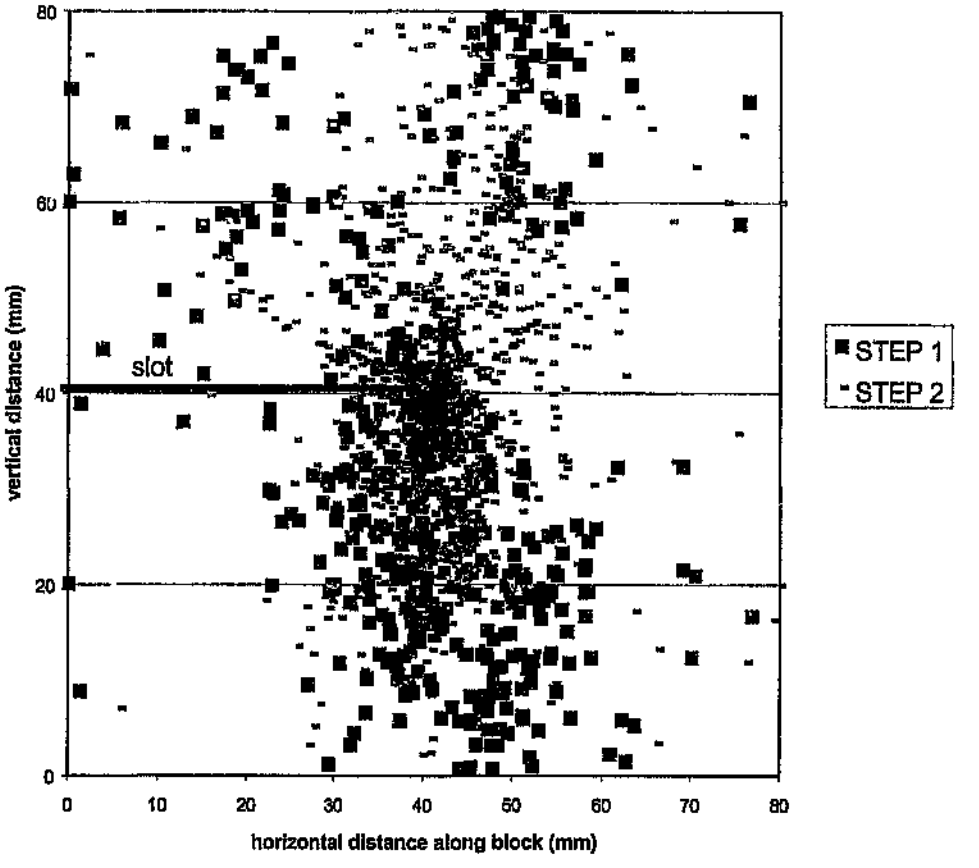
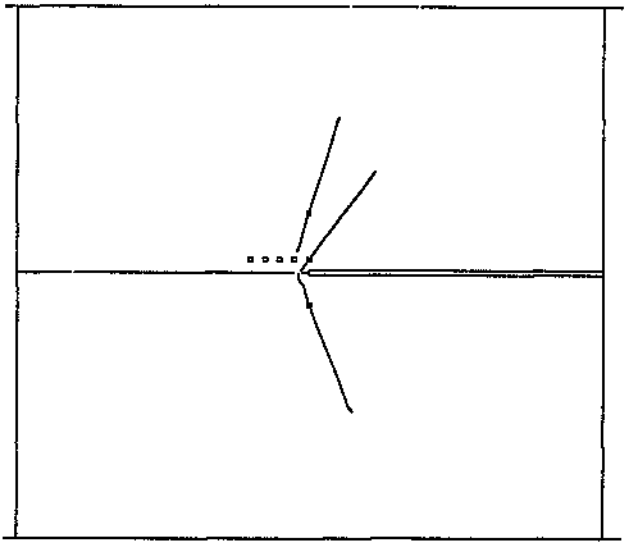


Figure 8.1.1.1: Locations of acoustic emissions determined in physical models using Black Reef Quartzite. a: block without discontinuity, b: block with parting planes

8.3. Comparison of physical and numerical models

In Figure 8.3.1a, the cases without parting planes, no closure was observed. The resulting fracture patterns show fractures extending behind the slot in both the hangingwall and footwall. In the hangingwall of the experiment (Figure 5.2.a) two fractures are evident, apparently initiating near the stope and extending out in two different directions. Similar fractures are observed in the numerical model. The vertical fractures ahead of the slot are not observed in the model as no seeds were placed at the top surface. In Figure 8.1.1, the fractures extend behind the advancing slot. Two fractures occur in the hangingwall at angles of 70° and 79° to the slot. In the footwall, a single fracture is angled at 81° to the slot. These crack angles are very close to those predicted in the model which are 71° and 80° in the hangingwall and 74° in the footwall, as shown in Figure 8.3.1.b. On the parting plane in the hangingwall of the test sample, there appears to be a slight shift of the fracture from left to right of about 2mm across the parting plane, and another fracture extends almost vertically to intersect with the boundary.

a:



b:

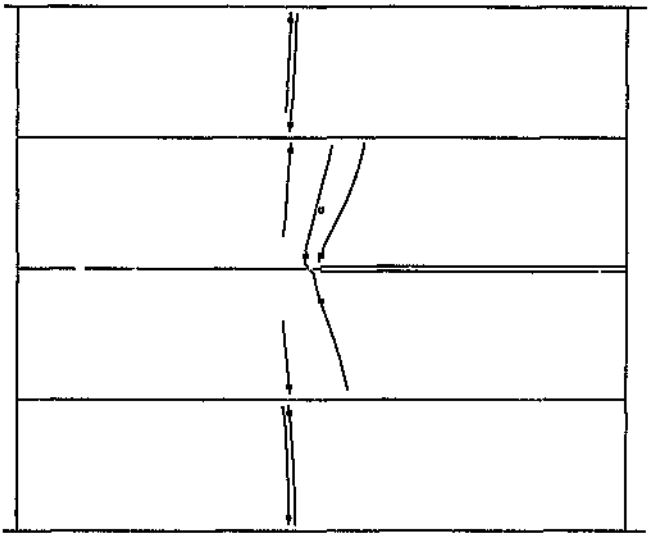


Figure 8.3.1: Fracture patterns predicted in numerical simulations of Black Reef Quartzite blocks. a: block without discontinuity, b: block with parting planes

The direction of fracture growth is not clear from the physical model, but comparison of the AE results (Figure 8.1.1.1b) with the numerical modelling (Figure 8.3.1.b) suggests that that each crack has grown downwards, one from the top boundary and the other from the parting plane. This supports the numerical modelling of Napier and Hildyard (1992), who suggest that it is the presence of parting planes that causes extension fractures to initiate above and ahead of a stope and not in the high stress region at the stope face.

This also supports the modelling of Ozbay (1995). Ozbay modelled the same scenario using DIGS. The results can be seen in figure 2.4.2. The tension growth rule is specified. Fracture was seen to be initiating from the layer interfaces. Fracturing also occurred ahead of the face with the orientation in the direction of the stope. The same results can be seen in figure 8.3.1. The points of fracture initiation and fracture orientation agree with the results of this dissertation as well as the results published by Ozbay (1995) for the numerical simulations. The results obtained by Ozbay (1995) on physical experiments with layered interfaces correlates well with those results obtained in this dissertation. Figure 2.3.4. shows Ozbay's results for the physical tests carried out. As in the numerical simulations, fracture initiate both at the corner of the opening as well as at the boundaries of the layered interfaces in Ozbay's case and at the parting planes in figure 8.3.1. The fractures initiating at the parting planes form ahead of the face in both results, while the orientation is steep and in the direction of the stope. In Ozbay's case and in the case of the results presented in this dissertation, the fractures are both tensile fractures.

8.4. Observation of Principle stress Direction

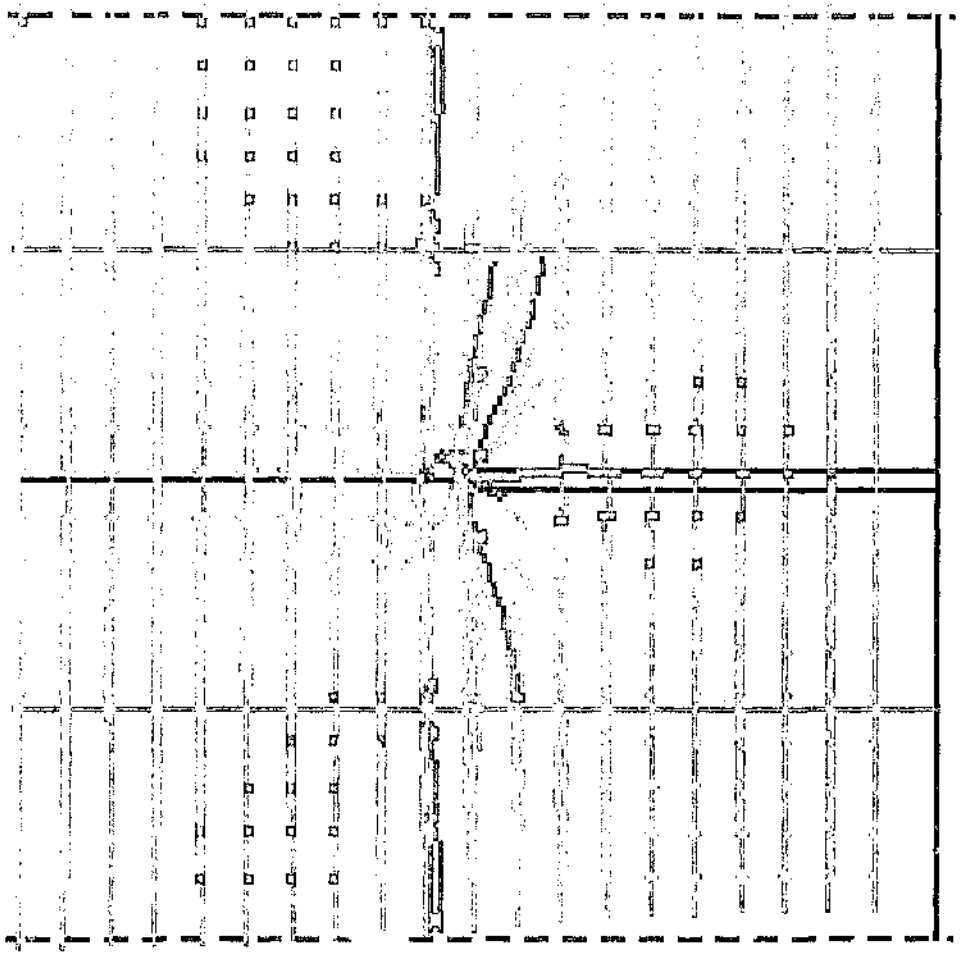


Figure 8.4.1. DIGS output of Stress Direction with an existing Parting Plane

The orientation of the stresses can be seen in figure 8.4.1. As is expected, the formation of the fractures are directly rel..ed to the direction of the stresses. There is a

good correlation between the direction of the stresses and the orientation of the tensile fractures. The grey lines indicating compressive stresses. The fractures initiating at the parting planes are also influenced by the direction of the major principle stress. This would indicate DIGS' ability to correctly calculate the stress around a stope as well as the stresses when being influenced by parting planes.

8.5. Fracture Initiation.

Figure 8.5.1 shows the data stored during the tests carried out on the parting plane sample. The results for step two are left out due to erroneous results which were obtained. Fracture initiation is illustrated in the graph where a substantial amount of strain occurs for very little or no increase in stress takes place. This is shown by a short horizontal line which occurs on the graph. For instance in figure 8.5.1. in the fourth step a moment of fracturing can be seen at 37 MPa where no increase in stress takes place, but a relatively large amount of strain occurs. The expected results of these recordings would have the fracturing of the sample taking place earlier on, or at a lower stress state, in the test for each progressive step. However, this is not the case, in step 1, fracturing takes place initially at 50 MPa, indicated by the short horizontal line. The same is true for step three where fracturing takes place at 50 MPa as well. In step four the initial fracturing takes place at 37 MPa which is lower than in steps one and three. Step five does not follow the same pattern as was expected. Instead of the initial fracturing taking place at a lower

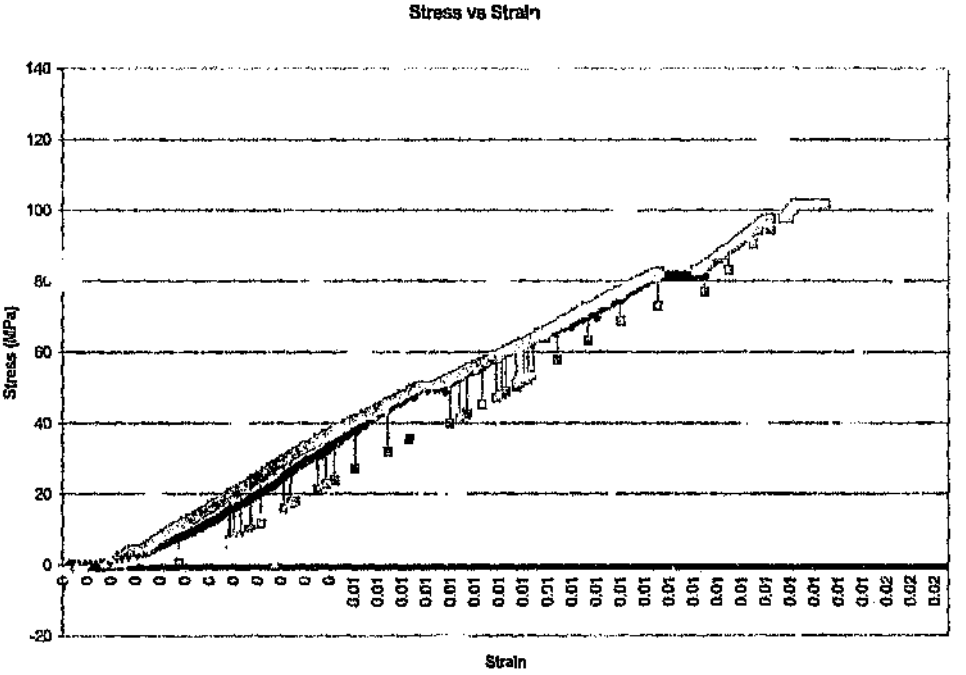


Figure 8.5.1 Stress vs Strain data for the parting plane sample. The purple line indicating step 1, the dark blue line indicating step 3, the yellow line step 4 and the turquoise the 5th step.

stress state than in steps one three and four, fracturing took place at a higher stress state than in all the previous steps. Fracturing took place at 75 MPa. According to the recordings of the experiments, fracturing took place mainly in two stages. Initially which has been described above and at another stage, except in step one. In step three this second stage of fracturing was at a stress of 80 MPa, for step four it was at 43 MPa and in step five fracturing for the second time took place at 106 MPa. A range of stresses in which fracturing took place can be determined. For this sample, the r ige was between 89 MPa and 123 MPa. These figures are all higher than what was recorded in the physical samples.

IX Conclusion and Recommendations

Modeling of the failure processes in rock is an essential addition to the analysis of observations of underground rock fracturing. The identification of mechanisms of deformation represents a basic step in the understanding of rock mass behaviour in different geological settings and at different working depths. Control of the rock mass deformation near a deep level stope and the avoidance of damaging incidents of violent rock failure requires a fundamental understanding of rock failure mechanisms.

The results of experiments on a solid block with varying stoping widths under triaxial loading conditions shows that closure of the stope and total closure of the stope results in different fracture formations. Where no closure of the stope occurs causes the fractures to form behind the stope face in both the hangingwall and the footwall. The fractures also appear to be tensile in nature. Where total closure of the stope occurs, the fractures form ahead of the stope face in both the hangingwall and footwall. The nature of the fractures appear to be shear fractures. Simulating the same scenario using DIGS gives similar results.

The results of experiments on blocks of rock containing a tabular slot under triaxial loading show that the presence of interfaces significantly alters the position and inclination of the resulting fractures. In the sample without discontinuities, the shear fractures which are observed to extend ahead of the stope in the experiments. The shear fracture criterion correctly predicts corresponding fractures in the numerical model. In the models with a pre-existing discontinuity, fractures extending from the tip of the slot are observed to terminate on the discontinuity. No fractures are evident

once the slot passes through the discontinuity suggesting that the deformation is occurring on the discontinuity. Similar trends are evident in the numerical simulations.

Fractures were apparently initiated at horizontal parting planes in both the physical and numerical models, indicating that the discontinuity can alter the stress distribution within the sample, depending on the interface properties. The analysis with a tensile fracture criterion correctly predicted the final fracture directions. The three dimensional acoustic emission location provides useful information regarding the sequence of fracture growth and the growth directions, which correlate well with the numerical simulations. The displacement discontinuity program DIGS can therefore predict the fracture patterns in these samples, and the influence of the various interfaces. The requirement to pre-select the seed point may however bias the final fracture pattern. The physical experiments demonstrate that the fracturing may occur in shear or tension depending on whether the slot is closed, or remain open. The logic to decide on the appropriate fracture criterion needs further consideration.

Inaccuracies with regards the fracture patterns formed between the physical and numerical model can, to some degree, be attributed to two important factors. Firstly, the samples characteristics used were taken from Dede (1996) who also used quartzite, however, quartzites from different areas may have slightly different characteristics.

Secondly, Dede (1996) gave the characteristics of a quartzite sample within a 90% confidence level. This allows for a 5 percent variation above and below the given

values. The number of combinations and permutations which can be obtained from a vast number of characteristics makes it difficult to accurately predict the true characteristics for each quartzite sample.

With the recent introduction of the DIGS tesselation version, this eliminates the need to select seed points, as a pre-defined grid of possible fractures is superimposed onto the given geometry. It is still necessary to select the correct parameters which determines the mode of failure. DIGS tesselation can accurately predict fracture patterns. The results above show DIGS' ability to predict the position of fracture initiation and the mode of failure given the correct failure parameters. DIGS tesselation is a step towards making DIGS a stand alone program without any prior knowledge of rock mechanics needed.

The findings of authors such as Brummer and Rorke as well as Joughin and Jager who found that the direction of fracturing around a deep level stope was closely related to the direction in which the major principle stresses was acting. The results from the numerical simulations backs up this theory. DIGS' simulations showed that a common direction was shared between the direction of the major principle stresses and the direction of the fracturing which took place.

Previous physical experiments carried out by Gay(1972) showed the presence of fracturing directly ahead of the face. This same phenomenon was not found in the experiments carried out in this dissertation. Fractures only occurred directly above and below the stope but not directly in front of the stope. The stress conditions to induce fracturing ahead of the face may not have been high enough for this to take place.

The results obtained using DIGS indicate that explicit modeling of fracture growth is feasible, but also shows that the modeling procedure is somewhat contrived in having to emplace appropriate seed growth sites at specific positions and following defined growth modes. More robust growth models should be developed that will not require the specification of possible fracture modes to simulate fracturing in mine stopes. As far as the future direction of this work is concerned, it is important to understand fracture processes in multiple layered materials. All the experiments and the numerical modeling in this work were carried out using 2-D plane strain models, however, in reality all fractures are in 3-D. Therefore these experiments need to be repeated, validated, calibrated and improved in 3-D as well.

X References

Brummer, R.K., Rorke, A.J., (1984) Mining Induced Fracturing around Deep Gold Mines Stopes. Research Report no 38/84

Dede, T., (1996) An Investigation into the Physical and Numerical modeling around underground excavations.

Gay, N.C., (1972) Fracture Growth around openings in Thick-Walled cylinders of rock subjected to Hydrostatic Compression. International Journal of rock Mechanics mineral sciences and geomechanics.

Joughin, N.C., Jager, A.J., (1984) Fracture of rock at stope faces in South African gold mines. Chamber of Mines Research Organisation.

Kranz, R.L., (1983) Microcracks in rocks: a review. *Tectonophysics,* 100:449-480.

Legge, N.B., (1986) Rock deformation in the vicinity of deep gold mine longwall stopes and its relation to fracture. Ph.D. Thesis, University College, Cardiff.

Lockner D., (1993) The role of acoustic emission in the study of rock fracture. *Int. J. Rock Mech. Min Sci. & Geomech Abstr.* 30:7 pp 883-889.

Lockner, D.A., Moore D.E., Reches, Z., (1992) Microcrack interaction leading to shear fracture. *Rock Mechanics.* Tillerson and Wawersik (eds). pp 807-816. Balkema, Rotterdam.

Napier, J.A.L., (1990) Modelling of fracturing near deep level gold mine excavations using a displacement discontinuity approach. *Proceedings of Conference on Mechanics of Jointed and Faulted Rock.* 709-715. Vienna, Balkema, Rotterdam.

Napier, J.A.L., Hildyard, M.W., (1992) Simulation of fracture growth around openings in highly stressed , brittle rock. *Journal of the South African Institute of Mining and Metallurgy.* 92:6 pp 159-168.

Napier, J.A.L., Hildyard, M.W., Kuijpers, J.S., Daehnke, A., Sellers, E.J., Malan, D.F., Siebrits, E., Ozbay, M.U., Dede, T., Turner, P.A., (1995) Develop a quantitative understanding of rockmass behaviour near excavations in deep mines. *Final report to Safety in Mines Research Advisory Committee.* CSIR Division of Mining Technology.

Ozbay, M.U., Ryder, J.A., (1989) Investigations into foundation failure mechanisms of hard rock squat rib pillars. In proceedings ISRM-SPE

International symposium Rock at great depths, Pau, Balkema, Rotteradm, pp. 527-535.

Ozbay, M.U., (1995) Modelling of fracturing surrounding mine openings and pillars. Safety in Mines Research Advisory Committee Final Project Report 1995.

Sellers, E.J., (1997) Personal discussion on existing numerical codes.

Ackknowledgement

The support of the Safety in Mines Research Advisory Committee (SIMRAC)

under project GAP332 is gratefully acknowledged.

XI Appendix A

Data file from DIGS. From this data file the nature of the simulation can be determined. The rock properties can also be determined. This rock sample has a Young's modulus of 90 Gpa and a Poisson's ratio of 0.2. This is seen in the first line of the data file. CM is a crack property. These are the parameters

given for shear fracturing. CF is a case for tensile fracturing. This is a simulation to predict the fracture formation in the presence of parting planes. This is seen in the line beginning with SP PP 30. The co-ordinates of the parting planes follows on.

```
PR 90000.0   0.20  0.000  0.000    0.0    0.0    0.0    0.0    0.0
CM   0.0 35.1 35.0   5.0   0.0 32.0   0.0   5.0   0.0   0.0   0.0
CQ   0.0   0.0 20.0   5.0   0.0 20.0   0.0   0.0   0.0   0.0   0.0
CW   0.5   0.0   0.0   0.0   0.0   0.0   0.0   0.0   0.0   0.0   0.0
CF   0.09999.0 35.0   5.0   5.0 30.0   0.0   1.0   0.0   0.0   0.0
CI   0.0   0.0   1.0   0.0   0.0   1.0   0.0   0.0   0.0   0.0   0.0
Ci   0.0   0.0   1.0   0.0   0.0   1.0   0.0   0.0   0.0   0.0   0.0
CP   0.0   0.0 20.0   0.0   0.0 20.0   0.0   0.0   0.0   0.0   0.0
CLCST    0.000    0.000NT  -27.000  -27.000
CRCST    0.000    0.000NT  -27.000  -27.000
C1CST    0.000    0.000NT  -27.000  -27.000
C0CST    0.000    0.000NT    0.000    0.000
C2CST    0.000    0.000NT  -80.000  -80.000
CbCST    0.000    0.000N-    0.000    0.000
CBCST    0.000    0.000N-    0.000    0.000
C3CST    0.000    0.000N+    0.068    0.068
C4CST    0.000    0.000N+    1.000    1.000
FO/
FNBLA6PP7.SAV
FCBLA6PP7.CFG
#I  1 100 60   500   0.1   0.0   0.4
S3 TOP 30   0.00   0.00  80.00   0.00   0.0   0.0     T   TT
SiLEFT 30   0.00   0.00   0.00  80.00   0.0   0.0     T   TT
SIRITE 15  80.00   0.00  80.00  40.00   0.0   0.0     T   TT
SI RIT 15  80.00  40.00  80.00  80.00   0.0   0.0     T   TT
Sb BOT 30   0.00  80.00  80.00  80.00   0.0   0.0     T   TT
SB RSB 30  80.00  80.00 160.00  80.00   0.0   0.0     T   TT
S0 RST 30  80.00   0.00 160.00   0.00   0.0   0.0     T   TT
SR RSR 30 160.00   0.00 160.00  80.00   0.0   0.0     T   TT
SB LSB 30 -80.00  80.00   0.00  80.00   0.0   0.0     T   TT
S0 LST 30 -80.00   0.00   0.00   0.00   0.0   0.0     T   TT
SB LSR 30 -80.00   0.00 -80.00  80.00   0.0   0.0     T   TT
RX
RG 20 20   0.40   0.40   0.00   3.90   3.90   32.0   0.0
#I  2 100 60   500   0.1   0.0   0.4
SW MID 30  80.00  40.00  40.00  40.00   0.0   0.0     T   TT
SQIMID 34  34.00  40.00   0.00  40.00   0.0   0.0     T   TT
SQIMI1  1  40.00  40.00  39.00  40.00   0.0   0.0     T   TT
SQIMI2  1  38.00  40.00  37.00  40.00   0.0   0.0     T   TT
SQIMI3  1  37.00  40.00  36.00  40.00   0.0   0.0     T   TT
SQIMI4  1  36.00  40.00  35.00  40.00   0.0   0.0     T   TT
SQIMI5  1  35.00  40.00  34.00  40.00   0.0   0.0     T   TT
SP PP 30  80.00  20.00   0.00  20.00   0.0   0.0     T   GG
SP PP1 30  80.00  60.00   0.00  60.00   0.0   0.0     T   GG
```

```
RX
RG 20 20  0.40  0.40  0.00  3.90  3.90  32.0   0.0
#I  3 100 60   500   0.1   0.0   0.4
S4 TOP
RX
RG 20 20  0.40  0.40  0.00  3.90  3.90  32.0   0.0
#I  4 100  1   250   0.1   0.0   0.4
?F CR3  50  40.00  31.00   0.0   0.0  90.00  1.000     T    T
?F CR4  50  40.00  31.00   0.0   0.0 -90.00  1.000     T    T
?F CR5  50  40.00  45.00   0.0   0.0  90.00  1.000     T    T
?F CR6  50  40.00  45.00   0.0   0.0 -90.00  1.000     T    T
?F T31  50  40.00  38.00   0.0   0.0  90.00  1.000     T    T
?F T32  50  40.00  38.00   0.0   0.0 -90.00  1.000     T    T
?F FR1  50  38.00  38.00   0.0   0.0  90.00  1.000     T    T
?F FR2  50  38.00  38.00   0.0   0.0 -90.00  1.000     T    T
?F F11  50  36.00  78.00   0.0   0.0  90.00  1.000     T    T
?F F12  50  36.00  78.00   0.0   0.0 -90.00  1.000     T    T
?F F21  50  36.00  62.00   0.0   0.0  90.00  1.000     T    T
?F F22  50  36.00  62.00   0.0   0.0 -90.00  1.000     T    T
?F F31  50  36.00  58.00   0.0   0.0  90.00  1.000     T    T
?F F32  50  36.00  58.00   0.0   0.0 -90.00  1.000     T    T
?F  T1  50  36.00  22.00   0.0   0.0  90.00  1.000     T    T
?F  T2  50  36.00  22.00   0.0   0.0 -90.00  1.000     T    T
?F  T3  50  36.00  18.00   0.0   0.0  90.00  1.000     T    T
?F  T4  50  36.00  18.00   0.0   0.0 -90.00  1.000     T    T
?F  T5  50  36.00   2.00   0.0   0.0  90.00  1.000     T    T
?F  T6  50  36.00   2.00   0.0   0.0 -90.00  1.000     T    T
RX
RG 20 20  0.40  0.40  0.00  3.90  3.90  32.0   0.0
#I  5 100 50   250   1.1   0.0   0.4
RX
RG 20 20  0.40  0.40  0.00  3.90  3.90  32.0   0.0
#I  6 100  0   250   1.1   0.0   0.4
SWIMI1
RX
RG 20 20  0.40  0.40  0.00  3.90  3.90  32.0   0.0
#I  7 100 20   250   1.1   0.0   0.4
RX
RG 20 20  0.40  0.40  0.00  3.90  3.90  32.0   0.0
#I  8 100  0   250   1.1   0.0   0.4
SWIMI2
RX
RG 20 20  0.40  0.40  0.00  3.90  3.90  32.0   0.0
#I  9 100 20   250   1.1   0.0   0.4
RX
RG 20 20  0.40  0.40  0.00  3.90  3.90  32.0   0.0
#I 10 100  0   250   1.1   0.0   0.4
SWIMI3
RX
RG 20 20  0.40  0.40  0.00  3.90  3.90  32.0   0.0
#I 11 100 20   250   1.1   0.0   0.4
RX
RG 20 20  0.40  0.40  0.00  3.90  3.90  32.0   0.0
#I 12 100  0   250   1.1   0.0   0.4
SWIMI4
RX
RG 20 20  0.40  0.40  0.00  3.90  3.90  32.0   0.0
#I 13 100 20   250   1.1   0.0   0.4
RX
RG 20 20  0.40  0.40  0.00  3.90  3.90  32.0   0.0
```

```
#I 14 100  0   250   1.1   0.0   0.4
SWIMI5
RX
RG 20 20   0.40   0.40   0.00   3.90   3.90   32.0   0.0
#I 15 100 20   250   1.1   0.0   0.4
RX
RG 20 20   0.40   0.40   0.00   3.90   3.90   32.0   0.0
/
```

Author:Tomlin, Wayne.
Name of thesis:The physical and numerical modelling of fracture growth in underground excavations.

PUBLISHER:
University of the Witwatersrand, Johannesburg
©2015

LEGALNOTICES:

Copyright Notice: All materials on the University of the Witwatersrand, Johannesburg Library website are protected by South African copyright law and may not be distributed, transmitted, displayed or otherwise published in any format, without the prior written permission of the copyright owner.

Disclaimer and Terms of Use: Provided that you maintain all copyright and other notices contained therein, you may download material (one machine readable copy and one print copy per page)for your personal and/or educational non-commercial use only.

The University of the Witwatersrand, Johannesburg, is not responsible for any errors or omissions and excludes any and all liability for any errors in or omissions from the information on the Library website.